8-2022

# Aerodynamics and Vibrations of a Helicopter Rotor Blade

Mohammad Khairul Habib Pulok
mpulok@uno.edu

# Aerodynamics and Vibrations of a Helicopter Rotor Blade

A Dissertation

Submitted to the Graduate Faculty of the
University of New Orleans
in partial fulfillment of the
requirements for the degree of

Doctor of Philosophy
in
Engineering and Applied Science
Mechanical Engineering

by

Mohammad Khairul Habib Pulok

B.Sc., Rajshahi University of Engineering and Technology, 2011
M.S., Bangladesh University of Engineering and Technology, 2016

August 2022

# Dedication

To

**My Late Father**

who passed a dream of enlightenment and signified the importance of education and excellence in life

**My Mother**

who always encouraged me to listen to my mind to do things as I think good and to have faith in me

and

**My Siblings**

who continuously supported me and took care of my mother, without which I could not afford to leave my home country to pursue my higher education

## Acknowledgment

I would like to extend my gratitude to my advisor Dr. Uttam K Chakravarty, for his guidance, support, and encouragement during the whole journey of my Ph.D. Without his mentorship and motivation, finishing this work would not have been possible. Moreover, his guidance helped me all the time to continue my research and write this dissertation.

I would also like to express my sincere thanks to Dr. Paul Schilling, Dr. Martin Guillot, Dr. Juliette Ioup, and Dr. Leszek Malkinski for serving as committee members for my dissertation. Their insightful counsel was essential to improving the quality of this manuscript. I thank my fellow lab mates in the University of New Orleans Aerodynamics and Vibrations Group—Jose Enrique Rubio and Pratik Sarker, for the stimulating discussions and guiding me in experiments.

In addition, I am indebted to my colleague M Shafiqur Rahman for his continuous support, inspiration, and motivation. Also, I express my heartiest thanks to my friends in the same group Md Mosleh Uddin, Iftekhar Alam Riyad, Debabrata Mondal, Anvesh Nallabali, Sri Charan Reddy Gudigopuram, Gazi Abu Raihan, and Oluwatosin Ojo for the excellent time we had in the lab. I am also thankful to Taylor Weidman, a Mechanical Engineering Technician, and Byron Landry, a Technician of the College of Engineering at the University of New Orleans, for their support in conducting the laboratory experiments.

Last but not least, I would like to thank my family: my mother, Sufia Razzaq, for being the driving force of my dreams, my siblings for being my strength, and my uncles for bringing me up after losing my father at an early age. Without my family and friends' support, I would not be able to finish this dissertation successfully.

This research is supported by the NASA EPSCoR Research Infrastructure Development (RID) grant (Contract No. LEQSF-EPS (2020)-RAP-29)). I would like to thank Dr. William Warmbrodt, who was the NASA technical monitor, for the work reported in this dissertation. The suggestions of Dr. Warmbrodt were helpful for this dissertation.

# Table of Contents

## List of Figures

## List of Tables

**Nomenclature**

| | |
|---|---|
| $C_D$ | coefficient of drag |
| $C_L$ | coefficient of lift |
| $V$ | velocity |
| $V_x$ | velocity in *x*-direction |
| $V_y$ | velocity in *y*-direction |
| $V_z$ | velocity in *z*-direction |
| $V_\infty$ | freestream velocity |
| $V_\theta$ | tangential or swirl velocity |
| $V_Z$ | axial velocity |
| $V_r$ | radial velocity |
| $\vec{V}_{loc}$ | local velocity |
| $\vec{V}_{ind}$ | induced velocity |
| $U$ | deformation |
| $U_x$ | deformation in *x*-direction |
| $U_y$ | deformation in *y*-direction |
| $U_z$ | deformation in *z*-direction |
| $\alpha$ | angle of attack |
| $\psi$ | azimuth angle |
| $E$ | modulus of elasticity |
| $\rho$ | density |
| $\nu$ | Poisson's ratio |
| $\mu$ | dynamic viscosity |
| $L$ | characteristic length |
| $l$ | length of the rotor blade |
| $c$ | chord length of the airfoil |
| $\vec{u}$ | flow velocity vector |
| $\vec{u}_g$ | drag force |
| $\Gamma$ | diffusion coefficient |
| $\bar{r}$ | nondimensional radius |

| | |
|---|---|
| $r$ | radial location |
| $r_c$ | vortex core radius |
| $\alpha$ | constant |
| $n$ | integer |
| $\vec{\omega}$ | vorticity vector |
| $\vec{V}$ | local velocity field |
| $\vec{r}$ | position vector |
| $t$ | time |
| $\psi_\omega$ | wake age |
| $\Omega$ | rotation |
| $\psi_j$ | location coordinate of $j^{\text{th}}$ vector |
| $z_{tip}$ | axial displacement |
| $y_{tip}$ | radial displacement |
| $R$ | maximum displacement |
| $k_1, k_2, C_T$ | Empirical coefficients in the wake models |
| $N_b$ | number of rotor blades |
| $\theta_{tw}$ | blade twist |
| $\Lambda$ | coefficient for the radial contraction |
| $A$ | constant |
| $B, C, m, n$ | empirical coefficients in the Kocurek & Tanglers wake model |
| $\lambda$ | contraction rate parameter |
| $S_\phi$ | source term of $\phi$ |
| $\partial V$ | boundary of the control volume, $V$ |

**Abbreviations**

| | |
|---|---|
| 2-D | two-dimensional |
| 3-D | three-dimensional |
| CAD | computer-aided design |
| CFD | computational fluid dynamics |
| DIC | digital image correlation |
| DFT | discrete Fourier transform |
| FFT | fast Fourier transform |
| FRF | frequency response function |
| FE | finite element |
| FSI | fluid-structure interaction |

# ABSTRACT

The nature of the aerodynamic environment surrounding a helicopter causes a significant amount of vibration to its whole body. Among different sources of vibrations, the aerodynamic loading on the main rotor blade is the major contributor. Therefore, analyzing a rotor blade's vibration characteristics and aerodynamic behavior becomes essential. The vortex characteristics and the wake surrounding a helicopter rotor blade play an important role because they affect the aerodynamic behavior of the rotor blade. An advanced mathematical and computational model of rotor wake and blade vortex gives a better understanding of the helicopter rotor dynamics. This study develops computational models of a helicopter rotor blade to obtain the vibration characteristics and aerodynamic behavior. In addition, a mathematical model of the wake is also used, consisting of the fundamental wake geometry. A Bo 105 helicopter rotor blade is considered for computational aerodynamic analysis. A fluid-structure interaction model of the rotor blade with surrounding air is developed, where the finite element model of the blade is coupled with the computational fluid dynamics model of the surrounding air. The fluid-structure interaction model analyzes aerodynamic coefficients, velocity profiles, and pressure profiles. The resonance frequencies and mode shapes are also obtained by the computational method. A small-scale model of the rotor blade is manufactured, and an experimental analysis of similar contemplation is conducted to validate the numerical results. Wind tunnel and vibration testing arrangements are used for the experimental validation of the aerodynamic and vibration characteristics, respectively. The computational results show that the coefficient of lift increases with the angle of attack up to a critical value. The coefficient of drag also increases with the angle of attack. The elastic rotor blades are subjected to coupled flapping, lead-lag, and torsional (triply coupled) deflections. The resonance frequencies and mode shapes in each direction vary

with the size and shape of the rotor blade and the mode number. The wake and vortex analysis showed that the swirl velocity is minimum, and the axial velocity is maximum at the vortex center. The axial velocity decreases, and swirl velocity increases with increasing the distance from the vortex center to the core radius.

**Keywords:** Rotor wake; vortices; vibration analysis; composite rotor blade; forward flight; numerical solution; finite element method; unsteady aerodynamics

# CHAPTER 1

# Introduction

A helicopter's vertical take off and landing capacity made it a prolific and essential way of transport in many areas, including military operations, medical emergencies, firefighting, and transportation of personnel and equipment. A few significant benefits of helicopters over fixed-wing aircraft are the capacity to hover for an extended amount of time, low-speed maneuverability, and the ability to take off and land in any congested area. In addition, the spinning motion of the helicopter rotor produces lift force opposite to the helicopter's weight to hover and maneuver. This chapter begins with the fundamentals of the aerodynamics of helicopter rotor and outlines the background of this study. The prospects and possible applications of the research will be discussed after that.

## 1. 1 Fundamentals of Helicopter

A helicopter is a flying machine that uses the rotor blade's rotation to generate lift, propulsion, and control. The helicopter rotor blades rotate about the vertical axis maintaining a horizontal or nearly horizontal plane. Interaction of the rotor surfaces with the air causes the generation of aerodynamic forces. The helicopter can hover at a particular elevation, take off and land vertically in any congested area; therefore, helicopters are preferable in many applications compared to fixed-wing aircraft. Multiple forces are generated and applied in a helicopter flight, which makes it a complicated flying machine. Figure 1.1 shows the force balance in the helicopter for a general flight condition.

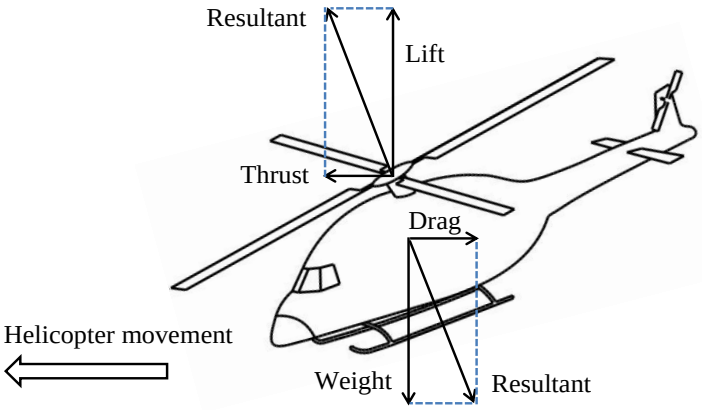


Fig. 1.1. A helicopter in a general flight condition with the force balance (Sarker, 2018)

## 1.2 Helicopter Rotor

Applied forces and moments are originated from multiple sources in a helicopter, including the rotary engine components, the steady and unsteady aerodynamic environments, and the interaction between the rotor blades. Helicopters are required to produce propulsive force to oppose the rotor drag in forward flight as it is needed to be capable of translational flights. The propulsive force is obtained from the rotor, tilting the thrust vector forward for at least the low speeds. The forces and moments generated in an aircraft control the position, altitude, and velocity are mostly originated from the rotor. The major three forces in any flying machine, i.e., the lift, propulsion, and control forces, originated mainly from different aerodynamic surfaces in a fixed-wing aircraft. However, the rotor produces all three types of forces in a helicopter. Usually, two or more equally spaced identical blades are attached to a central hub for any conventional helicopter rotor. The helicopter rotor can be described as a state subjected to six generalized forces and moments for any flight, varying magnitudes with different rotor configurations and flight conditions. As the rotor blade change their positions concerning the azimuth angle, the forces and moments of one blade are also available to the other blades. In

addition, the exceptionally high centrifugal force generated from the rotation of the blade keeps the blade almost straight, making the blade's rotation the rigid body motion. Therefore, the basic motions of each blade are categorized into three unique DOFs of motion, which are—the flapping, the lead-lag, and the torsional motions described in Fig. 1.2.

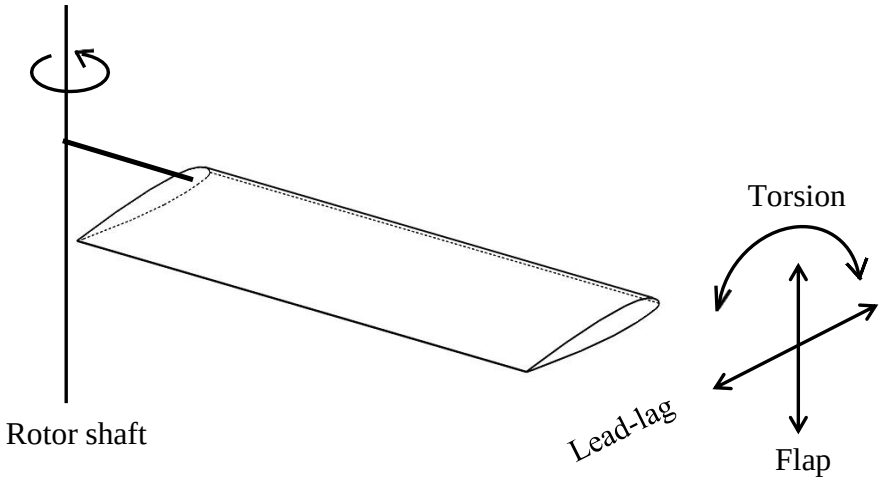


Fig. 1.2. Fundamental helicopter rotor blade motions

Three different aerodynamic loadings cause the three DOFs of motion: the lift force creating the flapping motion, the drag force creating the lead-lag motion, and the pitching moment, which creates the torsional motion. To understand the aeromechanics of the helicopter's flight comprehensively, the knowledge behind the mechanism of generation of these forces and moments is required. It is evident that to fly; an object must generate lift, a force that tends to move the object upward. Lift is usually generated by wings having an airfoil-like cross-section for both the fixed and rotary-wing aircraft. However, unlike a fixed-wing aircraft, a helicopter does not have to move quickly through the air to have a lift. Instead, a helicopter generates lift by moving the air over its spinning rotor blades at a certain speed. Wings create lift because of a relationship between the speed of the relative air and the pressure in the air, known as the

Bernoulli's principle. Bernoulli's principle states that the pressure goes down when the airspeed goes up. In the same way, when the airspeed goes down, the pressure goes up. The airfoil-like cross-section is curved at the top and relatively flat at the bottom. Therefore, as the helicopter blade rotates, the airfoil shape makes the airflow over the top move faster than at the bottom. As a result, there is less air pressure on top of the wing compared to the bottom, as shown in Fig. 1.3. The net pressure difference causes suction to move the wing in the upward direction, and thus lift is generated.

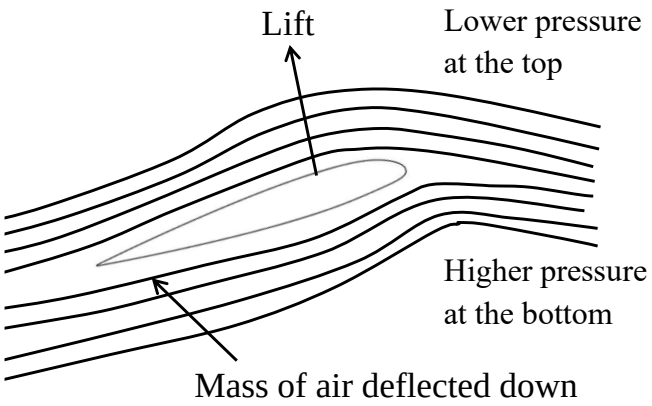


Fig. 1.3. The lift generation principle for the helicopter

Sometimes, the term 'thrust' is used in helicopter aeromechanics in parallel to 'lift'. However, the actual meaning of thrust differs from lift depending on the specific flight regime of the helicopter. In any flight condition with the respective orientation of the helicopter and its rotor blades, there is a net 'resultant' force which always acts perpendicular to the rotor disk plane. For the hovering flight, the lift itself is the resultant force that acts perpendicular to the rotor disk plane, which can be termed the thrust. However, for forward or other level flights, the rotor disk plane is tilted by a certain angle concerning the vertical axis to generate the propelling force for the helicopter. Then, from Fig. 1.1, the resultant force acting perpendicular to the rotor

disk plane is decomposed into the vertical force components, known as the lift and the horizontal component, which generates the propelling force. This horizontal force component is known as the thrust for forward or level flights. A helicopter's thrust can be forward, rearward, sideward, or vertical. The direction in which the helicopter will move is determined by the lift and thrust resultant. The solidity ratio of a specific helicopter rotor measures the potential of a rotor system to provide thrust and lift.

The lift generated by the helicopter rotor blade depends on the following factors:

1) Speed of the airflow

2) Density of the air

3) The rotor blade planform area

4) The angle of attack (AoA)

The lift is generated when an object changes the flow direction of a fluid or when the fluid is forced to move by the object passing through it. The rotor blade must be pitched up to deflect the air downwards, creating a positive lift that the pilot controls. However, with the pitch angle change, the AoA is also changed. The AoA is defined as the angle at which the rotor blade airfoil meets the oncoming airflow, defined as the relative airflow, a combination of the downwash and the tangential airflow shown in Fig. 1.4.

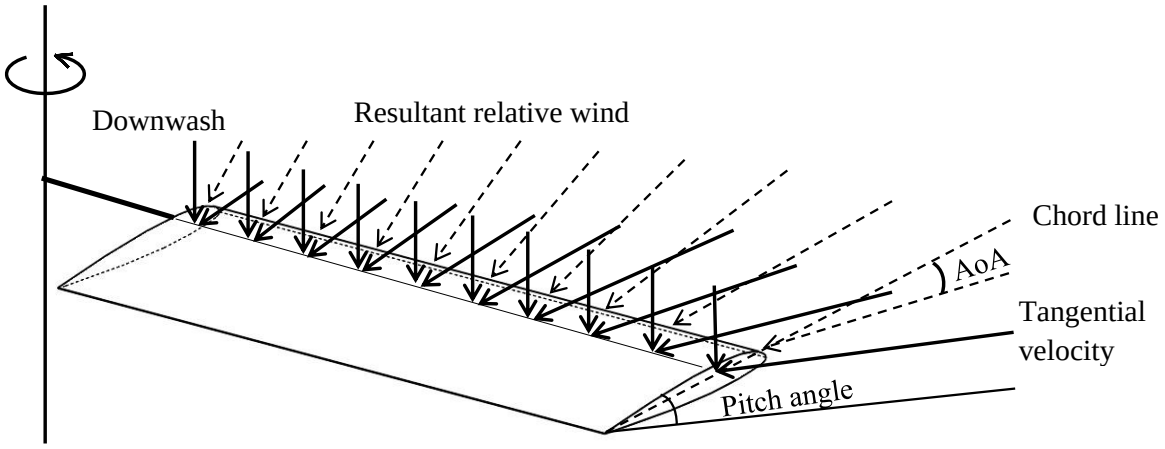


Fig. 1.4. Generation of lift, drag, and pitching moment in a typical helicopter rotor blade

As the helicopter moves, a force is generated that tends to resist the movement of a helicopter through the air. During the hovering flight, this force comes only from the rotational motions of the blades through the air. Nevertheless, for forward flight, this force comes from the blades' rotational motions and the fuselage's motion propagating through the air. This resistive force is the drag, and the engine power must overcome the overall magnitude of the drag. The overall drag force is a combination of the lift-induced drag and the profile drag, which always acts parallel to the relative wind. The profile drag is developed from the frictional resistance of the blades passing through the air. It does not change significantly with the airfoil's AoA but moderately increases when airspeed increases. Lift-induced drag comes from the contribution of the lift force, which is not exactly vertical. In forward flight, the parasite drag is generated due to the movement of the helicopter body through the air mass and is proportional to the relative airspeed. The non-lifting components of the helicopter, such as the cabin, rotor mast, tail, and landing gear, contribute to the parasite drag, which becomes the significant drag in high-speed forward flights.

The pitching moment for an airfoil is generated due to the aerodynamic lift force on the airfoil and the movement of the airfoil type through the air. The lift force is the distributed force assumed to act through the aerodynamic center. If the shear center of the airfoil cross-section does not coincide with the aerodynamic center, the lift force contributes to one part of the pitching moment. Another part of the pitching moment comes from the motion of the airfoil through the air, which depends on the Reynolds number. For this case, depending on the airfoil type, the pitching moment coefficient is calculated from the chart for a specific airfoil shape. However, as the AoA changes for a cambered airfoil, the pitching moment coefficient changes slightly over the whole operating range of the AoA. For helicopter aeromechanics, the 1/4th chord point is normally used as the point through which the pitching moment occurs and is considered the aerodynamic center.

### 1.3 Different Types of Helicopter Rotors

The governing equations of motion for a specific flight condition need to be formulated to investigate the helicopter's vibration characteristics. Solutions to the governing equations of motion are termed the boundary value problems, which require appropriate boundary conditions (BCs) to solve. Some of those BCs are determined directly from the end conditions of the helicopter rotor blades. The end condition, where the rotor blade is connected to the central hub, i.e., the blade's root, is different for different helicopter models. The response of the rotor blade subjected to the aerodynamic forces and moments is governed by the blade root condition. The mechanical arrangement of the central rotor hub to accommodate the flapping and the lead-lag motion of the blade provides a fundamental classification of rotor types which is discussed below.

### *1.3.1 Fully Articulated Rotor*

Generally, this rotor system is for helicopters with more than two blades. In the fully articulated rotor system, the blades are attached to the hub with flapping (moving up and down about an inboard mounted hinge), lead-lag (moving back and forth in the plane), and feathering (rotating about the pitch axis to change lift) hinges. Each blade motion is related to the others. This flapping hinge is designed to compensate for the dissymmetry of lift and might be located at varying distances from the rotor hub. Examples are Sikorsky S-300, AgustaWestland AW 109, etc.

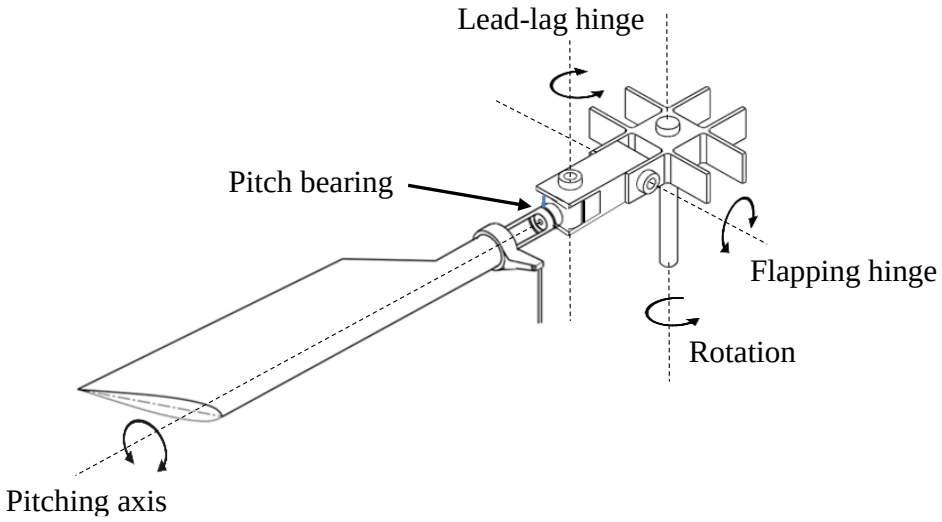


Fig. 1.5. Fully articulated rotor system (Sarker, 2018)

### *1.3.2 Semi-Rigid/ See-Saw/ Teetering Rotor*

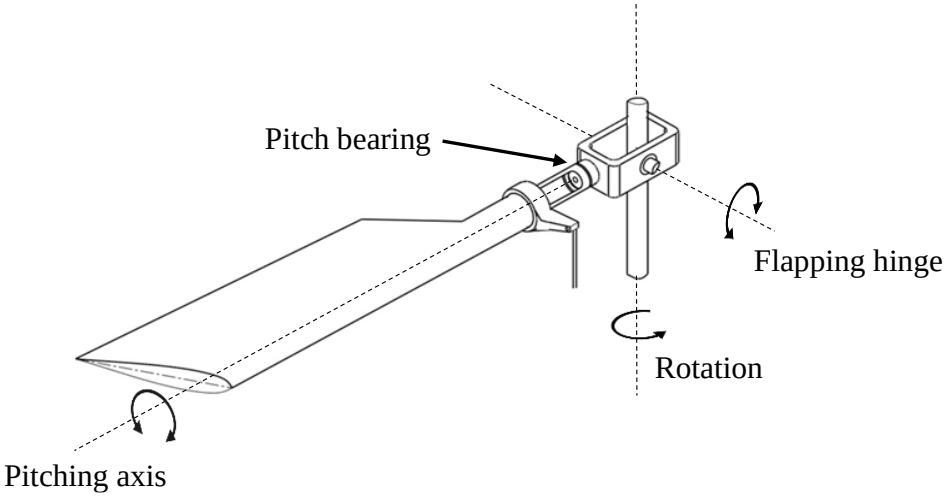


Fig. 1.6. Semi-Rigid rotor system (Sarker, 2018)

Semi-Rigid rotor systems are used in helicopters with two blades. The two blades are rigidly mounted to the main rotor hub. The main rotor hub is free to tilt concerning the main rotor shaft on what is known as a teetering hinge. This allows the blades to flap together as a single unit; as one blade flaps up, the other flaps down. The rotor has no lead-lag hinges; therefore, the force that tends to create the lead-lag motion is absorbed by the blade flex. The semi-rigid rotor has a feathering hinge to change the pitch angles of the blades. Examples are Bell 47, Robinson R22, etc.

### *1.3.3 Hingeless/Rigid Rotor*

The blades are flexibly attached to the hub without flap or lag hinges, although often with a feathering bearing or hinge. Loads from flapping and lead-lag forces are accommodated through rotor blades flexing rather than hinges. By flexing, the blades themselves compensate for the forces. The blade is attached to the hub with a cantilever root restraint so that no deflection occurs at the root and all kinds of bending motions occur in the remaining part of the blade.

Thus, the hingeless rotor, also known as the rigid rotor, eliminates the danger of mast bumping inherent in the teetering rotor. Examples are MBB Bo 105, Eurocopter EC 135, etc.

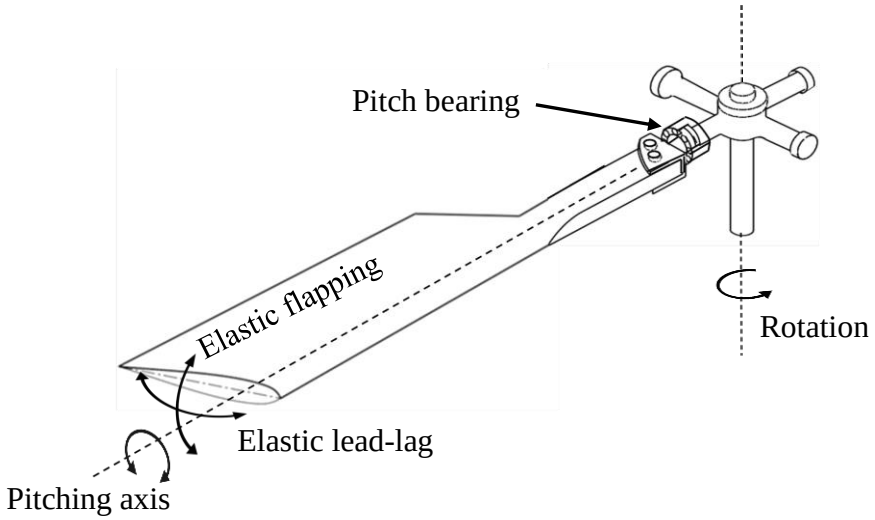


Fig. 1.7. Hingeless rotor system (Sarker, 2018)

**1. 4 Vibration in the Helicopter**

The aerodynamic forces are the reason the helicopters fly, but they can also cause vibration, which is detrimental to the life and safety of a helicopter. Rotation of the rotor blade may cause any imbalance of rotating mass or movement, which is another reason for vibration. Apart from these, unsteady aerodynamics and relative movement of connected parts may cause vibration. It is almost impossible to eliminate the vibration because the sources of vibrations are linked to the flying mechanism. Instead, an efficient control system could work to reduce the vibration and its detrimental effects. However, measuring and analyzing the modal characteristics are the most important prerequisite to start controlling vibration. Several sources, including the main and the tail rotor, engine, and gearbox, cause and contribute to the overall vibration. However, the main rotor is the primary source of vibration and noise.

### 1. 5 Aerodynamics of Helicopter

The airfoil shape cross-section of the helicopter rotor blade makes the surrounding airflow over the top faster than the bottom, which causes a lesser air pressure at the top of the wing compared to the bottom. Therefore, a pressure difference causes suction to move the wing in the upward direction, thus generating lift. The lift generation by a helicopter rotor blade depends on a few factors, including the airflow speed, the rotor blade planform area, density of air, and the angle of attack. A resistive force acts opposite when the helicopter moves forward, defined by drag. The drag force is generated from the frictional resistances of the blades passing through the air. The component of the lift force, which is not exactly vertical, also contributes to the drag force. The movement of the helicopter body through the air mass also causes drag force. The engine power to move the helicopter should overcome the overall magnitude of the drag. Aerodynamic lift force on the airfoil and the movement of the airfoil through the air causes the pitching moment.

### 1. 6 Motivation of the study

Helicopters are popular vehicles for many applications due to numerous reasons, including vertical take off and landing ability, hovering capacity, and low-speed maneuverability. Helicopters play an important role in military operations, medical services, private passenger-carrying, and many other areas where fixed-wing aircraft are not feasible. A helicopter is a complex flying machine composed of several complicated parts with dynamic loads from different directions. The rotor system is one of the most important segments, responsible for keeping the vehicle flying. Due to significant duration during vertical take off and hovering situations, the rotor system needs to be operationally safe and efficient. The rotor blades are the primary source of expected aerodynamic force generation. But different types of aerodynamic

loading cause vibration in the rotor blade. This vibration harms the flying machine's rotor life, safety, and efficiency. Therefore, analyzing aerodynamic loading and vibration characteristics is essential.

### 1.7 Literature Review

Different aerodynamic surfaces provide different sources of lift, propulsion, and control forces in any fixed-wing aircraft. In contrast, all three are provided by the rotor in a rotary-wing flying machine in helicopters. Therefore, rotors are of paramount interest for helicopter researchers. It plays a significant role in the flying machine's operation, safety, and comfort. Researchers have recently been contributing to a helicopter rotor (Zhou and Huang, 2022; James et al., 2022; van der Velden et al., 2021; Roy, 2021) to analyzing its different aspects. Zhou and Huang (2022) presented a calculation method for the stealth design of helicopter rotor by studying the radar cross-section at different blade pitches. They observed a reduction in the radar cross-section of the rotor at linear control in comparison to the fixed control mode. James et al. (2022) introduced a sensor-based strain and shape measurement during a ground run, which paves the way for exploring more efficient experimental data in terms of the mechanical characteristics of a helicopter rotor. van der Velden et al. (2021) performed experimentally validated simulations using a Lattice-Boltzman-based solver to obtain aerodynamic and acoustic behavior in both the mean and unsteady flow conditions. In extending the study of rotor blade design, Roy (2021) investigated the design parameters of composite laminates to minimize the tip deflection and maximize the overall efficiency of a helicopter rotor blade.

Helicopter designers have been facing the trouble and difficulties associated with vibration since the beginning of their operation. Bramewell et al. (2001) developed the free vibration theory, where they considered the motion of the helicopter rotor blade as the rotation of

a flexible cantilever beam. Aksencer and Aydogdu (2015) analyzed the flapwise vibration of rotating composite beams using different composite beam theories and obtained the solution by the Ritz method. In hovering conditions, the stability of elastic bending and torsion of uniform cantilever rotor blades with variable structural coupling was investigated by Hodges and Ormiston (1976). Following that, Hodges et al. (1991) formulated the procedure for forecasting the natural frequencies and mode shapes of composite beams with arbitrary cross-sections using the finite element (FE) method. Sarker et al. (2016) conducted the vibration analysis of a composite helicopter rotor blade in hovering conditions. They performed a generalization of the method of lines to develop a robust numerical solution in terms of time-varying deflections and velocities to analyze the dynamic response of a hingeless helicopter rotor blade at hovering and forward flights (Sarker, 2018). Zaw et al. (2014) conducted a stability analysis of an unmanned aerial helicopter considering rigid body dynamics and developed the mathematical model using the minimum complexity helicopter simulation.

Hingeless rotorcraft have been subjecting to substantial research for many years because they are found to be more demanding than articulated rotors in dynamic design. Considering the flight requirement and material properties of the rotor blade, Bolkow GmBh began to develop its fiberglass hingeless rotor blade in 1961. Subsequently, Bo 105 was initiated in 1964 (Hohenemeser, 1974). Modeling the aerodynamics of helicopter rotor blades and measuring the aerodynamic loads have been a continuous process. Ho and Yeo (2017) predicted helicopter rotor blade load using a rotorcraft comprehensive analysis tool in steady level forward flight conditions and compared it with four different rotors. Walsh et al. (1987) described an optimization procedure for the aerodynamic design of a helicopter rotor blade that minimizes hover horsepower, assuring satisfactory forward flight performance. Koning et al. (2019)

presented an improved Mars helicopter aerodynamic rotor model for comprehensive analysis. They used a free wake analysis to generate a performance model of the Mars helicopter. Weiss et al. (2019) analyzed the effect of rotational forces on the rotor blade. They investigated the laminar-turbulent boundary-layer transition on the suction side of a Mach scale helicopter rotor blade in a climb. Unsteady flow phenomena create complexity in the helicopter rotor aerodynamics and its optimization technique. Bailly and Bailly (2019) presented a multi-fidelity optimization technique that was applied to the design of a helicopter rotor blade, improving its performance in forward flight.

Computational methods are effective in analyzing rotor performances, and a lot of researchers have been using numerical tools to outline the aerodynamics of the rotor blade. A joined multidimensional finite element (FE) approach was proposed by Hoseini and Hodges (2019) to exploit the computational efficiency of the reduced dimensional beam model along with the accuracy of three-dimensional continuum models. They analyzed the linear and nonlinear divergence and flutter for damaged high-aspect-ratio wings undergoing large deformations. The fluid-structure interaction (FSI) is one of the widespread multiphysics phenomena where a deformable or moving solid structure is surrounded by fluid flow. A coupling between the laws of fluid dynamics and structural mechanics are involved in the FSI analyses. Yang et al. (2015) developed the fluid-structure interaction model as the efficient numerical technique for simulating a rotorcraft flow field with overlapping grids. They solved the Reynolds-averaged Navier–Stokes equations using multigrid and time spectral methods. Writh et al. (2017) used standard FSI co-simulation interface MpCCI to analyze the flow around flexible wings and blades. They outlined the deformation, the pressure developed, and force effects on the solid blade due to fluid flow. Crook et al. (2017) considered a nonlinear aeroelastic

approach to couple the computational fluid dynamics (CFD) and computational structural dynamics solvers. They demonstrated the ability of their method to capture the complex three-dimensional rotor behavior by analyzing stability, flutter, and rotor aeroelasticity.

Although experimental performance analysis of helicopter rotors has always been challenging, researchers, including Wang et al. (2020), conducted wind tunnel experiments. A series of wind tunnel tests carried out an understanding of high-aspect-ratio aerodynamic phenomena, such as thrust reversal and dynamic stall in the reverse flow region (Wang et al., 2020). Shinoda (2004) conducted the wind tunnel experiment to investigate the wide chord blade-rotor system. The overall rotor performance of the small aircraft was not varied on their test data with the center of gravity shift. The effect of turbulent inflows on airfoil performance for a horizontal axis wind turbine at low Reynolds number flow was analyzed by Li et al. (2016). They investigated the aerodynamic characteristics and performances of the turbine.

Rotor harmonic airloads are generated from the rapid variation of flow around the rotor blade due to vortex wake. Riyad and Chakravarty (2018) analytically calculated the unsteady aerodynamic airloads, i.e., the lift, the drag, and the pitching moment, at a blade section for lower harmonics where the mathematical model was faster than the computational method without sacrificing any accuracy for lower harmonics. Madden (1967) illustrated the distribution of attack angles for the high-speed helicopter and mentioned the requirement of the variable strength wake to predict higher harmonic airloads correctly. In the case of a floating wind turbine rotor, aerodynamic performances were studied by Farrugia et al. (2016). Finally, the dynamic wake distortion model for helicopter maneuvering flight was developed by Zhao (2005).

The vortex shedding dominates the rotor blades and creates a highly complex flow field for the rotorcraft. Therefore, the rotor wake and blade vortex formation are significant to the

helicopter rotor dynamics. Rotor wake has been subjecting to substantial research for many years because it plays a vital role in helicopter aerodynamics. McAlister (2004) studied the rotor wake development during the first revolution. He distinguished the distribution of vorticity from the slightly elliptical swirl pattern. In his study, the vortex core radius increased slightly with wake age, whereas the large radius circulation looked to remain relatively constant. Many researchers have recently contributed to the area of rotor wake and vortex formation. Schwarz et al. (2019) used stereoscopic particle image velocimetry to measure the flow field around a free-flying model helicopter in ground effect. They performed the study for both the quasi-steady and unsteady maneuvering flights. Following that, different patterns, including recirculation, wall jet, and ground vortex flow, were quantitatively analyzed (Schwarz et al., 2020). Their research output provides a better understanding of the rotor-ground interactions in realistic flight situations.

The wake of a helicopter rotor is characterized by multiple structures, including the blade tip vortex, the rotor downwash, the blade shear layers, and the surrounding external flow. The wake is three-dimensional and generates an unsteady flow field. Uluocak et al. (2021) experimentally investigated the effects of tip anhedral on the tip vortex characteristics in hovering flight and on the aerodynamic performances of the helicopter rotor. Wolf et al. (2019) explored the wake of a subscale rotor in ground effect using the “Shake-The-Box” technique using time-resolved and volumetric flow-field measurements. The application of the volumetric flow measurement technique to a rotor wake was outlined in their study. Van der Wall et al. (2017) used a realistic swirl velocity profile to obtain a closed-form solution of rotor aerodynamics. The aerodynamic impact of a straight-line vortex lying in the plane of a rotor disk is solved in their study based on blade element/momentum theory. Venegas et al. (2021)

considered Joukowski's rotor model for a two-blade rotor. Their solution described a steep-descent helicopter flight regime for which the vortex structure is strongly deformed in the near wake and crosses the rotor plane. Sing and Friedman (2018) studied the application of the vortex method to coaxial rotor wake and load calculations in hover. They applied the viscous vortex particle approach to evaluate performance, wake evolution, and loads in hover for a coaxial rotor system. Brown (2000) worked on the numerical solution of the unsteady fluid-dynamic equations governing the generation and convection of vorticity through a domain enclosing the helicopter and, therefore, generated a computational helicopter rotor wake model. He used a vorticity conservation approach in conjunction with suitable vorticity flux-limited functions to overcome excessive numerical dissipation of vortical structure.

Researchers also contributed to analyzing different helicopter aspects in recent times. Zhou et al. (2022) simulated a probabilistic evaluation of the remaining life of a structural component of a helicopter. They used parametric modeling, boundary element method, finite element (FE) method, and machine learning approaches to realize the digital twin of complex structures. Escober et al. (2021) conducted a high-fidelity aeromechanical analysis using a computational fluid dynamics (CFD) solver for the coaxial Mars helicopter to predict the flight loads and understand the Martian aeromechanics. However, several complicated parts with dynamic loads from different directions on a rotorcraft make it a complex flying machine. The rotor system is one of the most critical segments responsible for flying. Therefore, the operational safety and efficiency of the rotor blade are a significant concern for helicopter researchers. The rotor blades are also the primary source of expected aerodynamic force generation. At the same time, different types of aerodynamic loading cause vibration in the rotor blade. This vibration harms any flying machine's rotor life, safety, and efficiency. Therefore,

analyzing different aspects of rotor blade performance, including the aerodynamic loading and vibration characteristics, has been a critical concern for many helicopter researchers. Bardera Mora and Matías García (2022) studied the rotor ground effect and frigate interaction using particle image velocimetry inside a wind tunnel. The measured velocity output used to predict the increment of flow asymmetry below the rotor increase with the proximity to a partial ground distance. Sarker and Chakravarty (2021) studied the dynamic response of a hingeless helicopter rotor blade analytically using the method of lines. They considered a Bo 105 rotor blade with standard parameters for the mathematical formulation of modal relations. The effectiveness of open-loop and active flow control in reducing helicopter rotor vibration is examined in the study of Patterson and Friedman (2022) using numerical simulations. The outcome of their study implies the significant control authority of the flow control actuators to modify the vibratory loads.

### 1. 8 Research Objectives

The main rotor has a significant contribution to the aerodynamic forces and vibration. Therefore, analyzing the performance of a rotor blade is essential. Vibration characteristics and aerodynamic forces must be thoroughly known to design and improve the performance of a rotor blade. Wake and vortex formation is also very crucial to helicopter aerodynamics. For this analysis, the Bo 105 helicopter is considered the base model because of the flexible nature of the rotor blades and the simplicity of the hingeless rotor to be used as a cantilevered beam end condition in the numerical analysis. The outcome of this analysis can be fruitful for the design purpose of the rotor blade and for the time and cost-saving numerical solution. Numerical solutions of fluid-structure interaction analysis are also required to be matched with the wake and

vortex characteristics obtained using empirical formulas. Keeping these in mind, the objectives of this analysis are sequentially broken down and are mentioned below:

a) Study of the free vibration characteristics of a hingeless helicopter rotor blade

1. To develop a FE model for estimating the natural frequencies and mode shapes for flapping, lead-lag, and torsional vibrations.

2. To model and manufacture small-scale rotor blade using the additive manufacturing process for experimental validation.

3. To conduct experiments using shaker experimental setup with the digital image correlation system to validate the finite element model.

b) Study of the aerodynamic behavior of a helicopter rotor blade

1. To develop an FSI model comprising the FE model of the rotor blade and CFD model of the surrounding air for estimating the aerodynamic coefficients.

2. To conduct wind-tunnel experiments with a small-scale rotor blade placed in a sting balance and obtain aerodynamic loads using a data acquisition system so that the FSI model can be experimentally validated.

c) Study of the wake generation and vortex formation of a helicopter rotor blade

1. To collect and utilize established empirical formulas for obtaining wake and vortex formation behavior.

2. To use the FSI model for obtaining the vortex formation and match them with the results obtained using empirical formulas.

# CHAPTER 2

# Methodology

## 2.1 Bo 105 Helicopter Rotor Blade

The Messerschmitt-Bölkow-Blohm Bo 105 helicopter rotor blade is flexibly attached to the hub without flap or lag hinges. Contrary to other rotor blades, loads from flapping and lead-lag forces are accommodated in a Bo 105 through rotor blade flexing rather than through hinges. Moreover, the blades themselves compensate for the forces by flexing. The hingeless rotor, also known as the rigid rotor as shown in Fig. 2.1, is perhaps the most significant feature of the Bo 105 rotorcraft. The flexibility of the rotor blades works to absorb movements typically requiring hinges in most helicopter rotor designs. As a result, the reliability of the Bo 105 rotorcraft is higher because of its shallow failure rate, and the hingeless rotor blade is partially responsible for the agility and responsiveness of the rotorcraft.

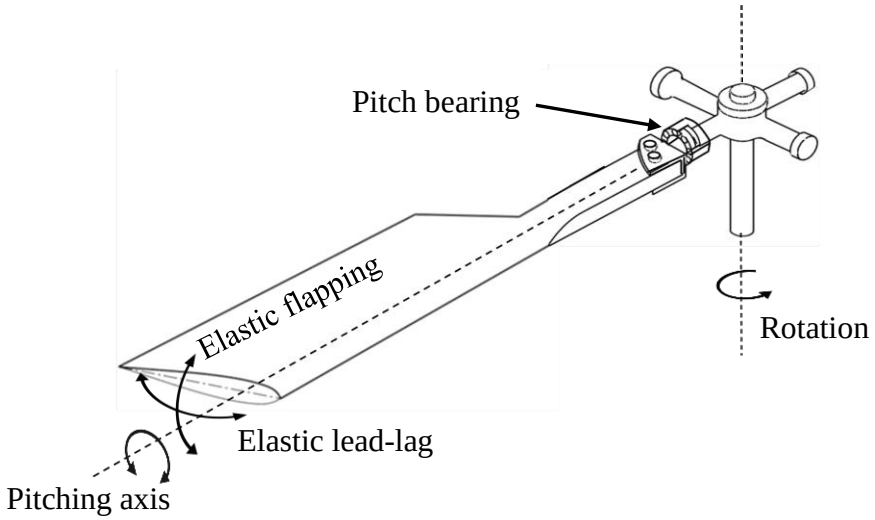


Fig. 2.1. MBB Bo 105 (Hingeless) rotor system (Sarker, 2018)

Because of the advantages of a hingeless rotor blade and the simplicity of its design, the Bo 105 helicopter rotor blade is considered for this study.

## 2.2 Background of Material and Geometry Selection

The history of helicopter blades dates to 1960 when the primary constituent materials of the rotor blades were laminated wood and fabric. Wood is an excellent material for the rotor blades; however, one disadvantage of wood is that it tends to absorb moisture, and therefore, the mass of the blades is altered. Metallic blades such as steel or aluminum appeared to have greater strength than wood; to overcome this problem. However, metallic blades possessed poor fatigue resistance and a low strength-to-density ratio. Also, when a metal blade was damaged or cracked in a critical area, it experienced a catastrophic failure with little warning. In the quest for a strong, lightweight, and reliable helicopter rotor blade material, it was found that no specific material was as tough as metal and light as wood. The only solution is to manufacture the blades composed of composite materials. The most attractive feature of composite materials is their highest strength-to-weight ratio. Following this, perhaps, the essential use of composite materials in the modern history of rotary-wing aircraft is their presence as the primary constituent materials. Also, composite materials are much easier to process and manufacture. They can be combined with adhesives, negating the need for riveting and simplifying the assembly, and can be manufactured using much cheaper tooling than metals.

Among various composites used as the constituent materials of the helicopter rotor blade, the carbon-epoxy, fiberglass-epoxy, and boron-epoxy composites are the most common. For all of them, the epoxy matrix (Ahmed et al., 2018) is reinforced with the fiber, where the volume fraction of the fiber and the epoxy can be varied. Sandwich-structured composite are developed with a thin layer of relatively stronger material and a thick core of different material. Pulok et al.

(2021) numerically demonstrated the stress-strain performance of a sandwich-structured composite and observed better performance than the isotropic counterparts. Moreover, different fibers in the composite blade give different directional stiffness properties, which can be used to control the aeroelastic deformation, known as aeroelastic tailoring. Therefore, modern helicopters have no alternative to using composite materials with suitable fiber orientations to beneficially affect the aerodynamic and structural performance. In this chapter, a model of the Bo 105 helicopter rotor blade cross-section is proposed made of composite and other materials representing the cross-section of a sandwich beam.

## 2.3 Material Properties and Geometry

The proposed geometry of the rotor blade for the vibration and aerodynamic analysis is similar to that of the MBB Bo 105 helicopter rotor blade. In addition, the cross-section profile resembles the NACA 23012 airfoil (Goulos et al., 2015).

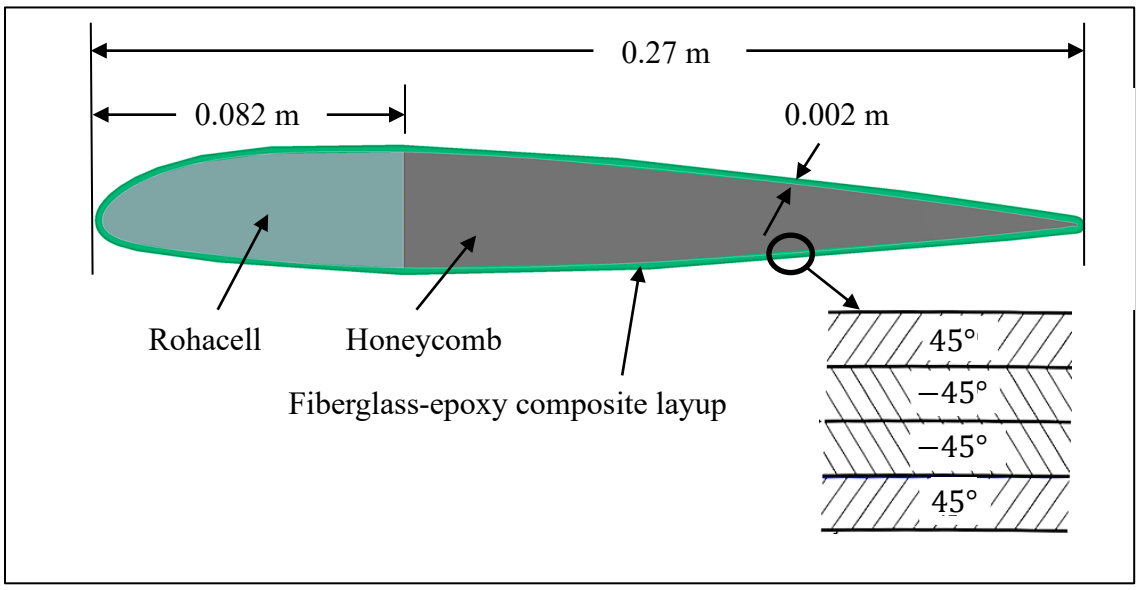


Fig. 2.2. Considered cross-section of the Bo 105 helicopter rotor blade

The geometry and material characteristics of the rotor blade considered in this study are predicted from Literature (Sarker, 2018; Sarker and Chakravarty, 2021; Pulok and Chakravarty, 2020) and are shown in Fig. 2.2 and Table 2.1. As shown in Fig. 2.2, the geometric construction gives the elemental components of a typical rotor blade cross-section. The composite shell acts as a balanced laminate composed of four plies with a high strength-to-weight ratio compared to the inner core of the cross-section, which is considered a sandwich beam cross-section. The outer shell composite of fiberglass-epoxy material formed a thickness of 0.002 m where the four layers of equal thickness (0.0005 m) are constructed with fiber orientation of $45°$, $-45°$, $-45°$, and $45°$.

Table 2.1. Parameters of the helicopter rotor blade

| | Parameters | Value |
|---|---|---|
| | Rotor | MBB Bo 105 |
| | Airfoil | NACA 23012 |
| | Length of the rotor blade, $l$ (m) | 4.61 |
| | Chord length of the airfoil, $c$ (m) | 0.27 |
| Fiberglass-epoxy composite | Density, $\rho$ (kg/m$^3$) | 2100 |
| | Modulus of elasticity, $E_1$ (Pa) | 45e9 |
| | Modulus of elasticity, $E_2$ (Pa) | 12e9 |
| | Shear modulus, $G_{12}$ (Pa) | 5.5e9 |
| | Poisson's ratio, $\nu_{12}$ | 0.28 |
| | Thickness, $h_{shell}$ (m) | 0.002 |
| Rohacell | Density, $\rho_r$ (kg/m$^3$) | 75 |
| | Modulus of elasticity, $E_r$ (Pa) | 105e6 |
| Honeycomb | Density, $\rho_h$ (kg/m$^3$) | 48 |
| | Modulus of elasticity, $E_h$ (Pa) | 128e6 |

A small-scale rotor blade is manufactured and modeled for experimental validation. The geometry and material characteristics of the small-scale rotor blade considered in this study for experimental validation are listed in Table 2.2.

Table 2.2. Parameters of the small-scale rotor blade

| Parameters | Value |
|---|---|
| Airfoil | NACA 23012 |
| Length of the rotor blade, $l$ (cm) | 12.05 |
| Chord length of the airfoil, $c$ (cm) | 2.61 |
| Materials considered | 3D Printed ABS Plastic |
| Density, $\rho$ (kg/m$^3$) | 1040 |
| Modulus of elasticity, $E_2$ (Pa) | 2e9 |
| Poisson's ratio, $\nu$ | 0.37 |

## 2.4 Computational Model

Two separate models are constructed for the computational analyses of the flow characteristics and vibration properties of the Bo 105 helicopter rotor blade: a solid model and a fluid model. The commercially available Ansys Workbench 2019 R3 package software is used for the computational analysis. Two sets of different numerical models are created − a small-scale rotor blade model for experimental validation and full-scale rotor blades. In each set, it is a combination of the FE model of the rotor blade and the CFD model of the surrounding airflow. The geometry, material, and surrounding environment of the small-scale FE and CFD models are considered so that it becomes comparable to the experimental arrangements used in this study. A Bo 105 helicopter rotor blade is considered in the computational models for the full-scale models. The transient structural FE model of the rotor blade and the fluid flow (fluent) CFD

model of the surrounding air are coupled for the 2-way multi-physics FSI analysis. The models are briefly described in the following sections.

### 2.4.1 Finite Element Model

At first, the commercially available SolidWorks 2020 software is used to generate solid models of both full-scale and small-scale rotor blades. Then the models are imported into the Ansys Workbench for the geometry construction of the FE models. Ansys Workbench, ACP (Pre) is used for generating composite layup of the outer shell, whereas Mechanical Model is used for the inner core of the rotor blade. Both meshed models are combined to form the FE model in the Modal analysis and Transient Structural analysis of the Ansys analysis systems. The material properties and dimensional information stated in Table 2.2 is used for the small-scale FE model. Similarly, the material properties and geometric information stated in Table 2.1 is used for generating the full-scale FE model. The blades are considered fixed at the root. The whole outer surface of the rotor blade is assigned as the fluid-solid interface for the analysis. The FE model of the rotor blade is shown in Fig. 2.3.

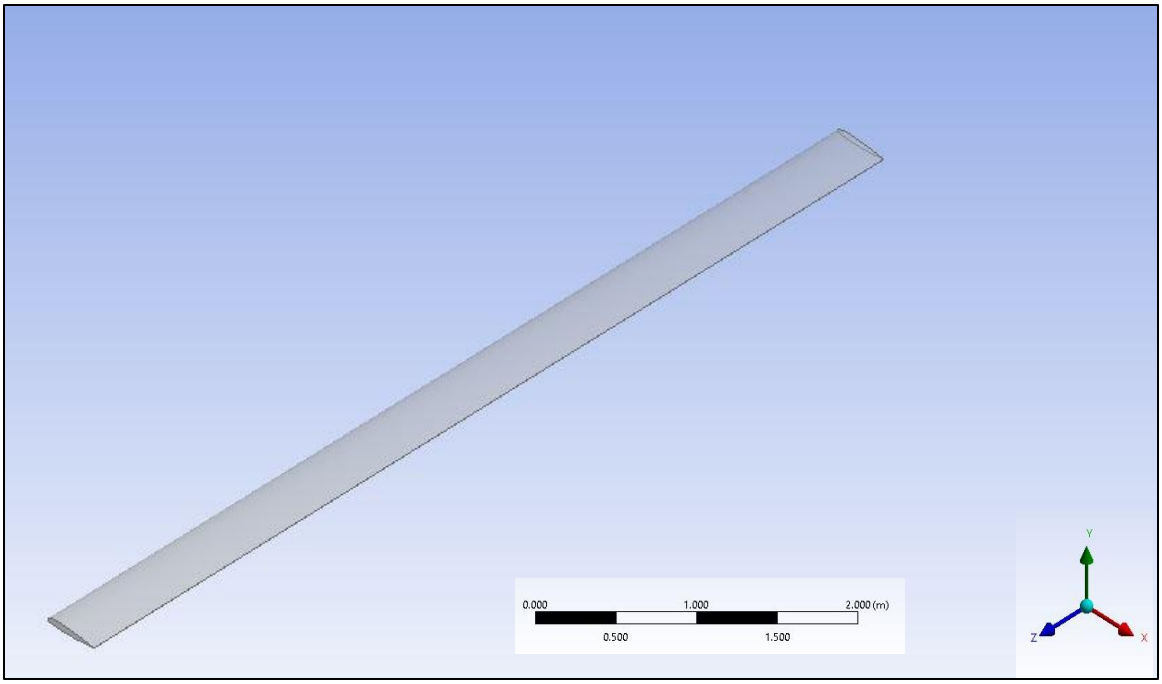


Fig. 2.3. FE Model of the Bo 105 helicopter rotor blade

For the FE analysis, 5000 linear tetrahedral mesh elements are used as shown in Fig. 2.4.

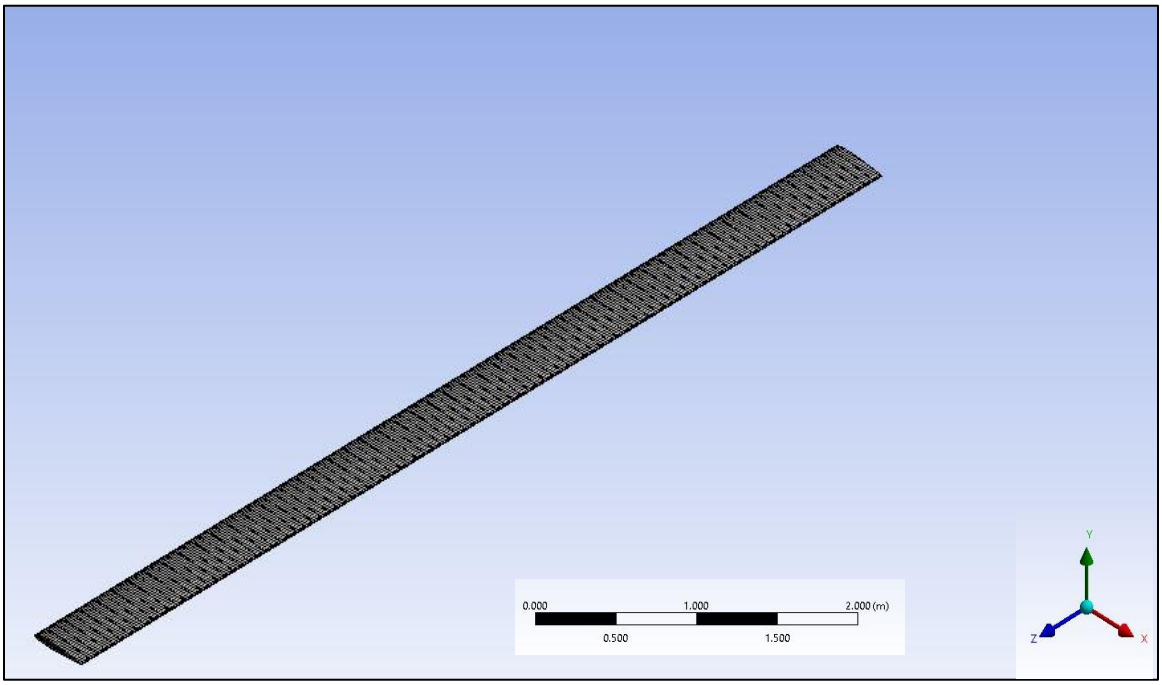


Fig. 2.4. FE Mesh of the Bo 105 helicopter rotor blade

Natural frequencies and mode shapes are obtained from the modal analysis of the FE model.

### 2.4.2 Computational Fluid Dynamics Model of the Surrounding Airflow

For both small-scale and full-scale CFD models, rotor blade geometry is shared with the FE model for creating a cavity of rotor blade inside the fluid domain. A rectangular volume of 30 cm × 10 cm × 40 cm is generated as a CFD domain for the miniature model with a small-scale rotor blade cavity at the center of the domain. Similarly, a rectangular volume of 8 m × 6 m × 8.5 m is generated as a full-scale model with the cavity of a full-scale Bo 105 helicopter rotor blade. The domain sizes are selected in such a way that there is no boundary effect. With these dimensions, the far-field and downstream boundaries are distant enough not to affect the flow behavior in the vicinity of the rotor blade structure based on domain size limits suggested for CFD studies. The fluid domain is shown in Fig. 2.5.

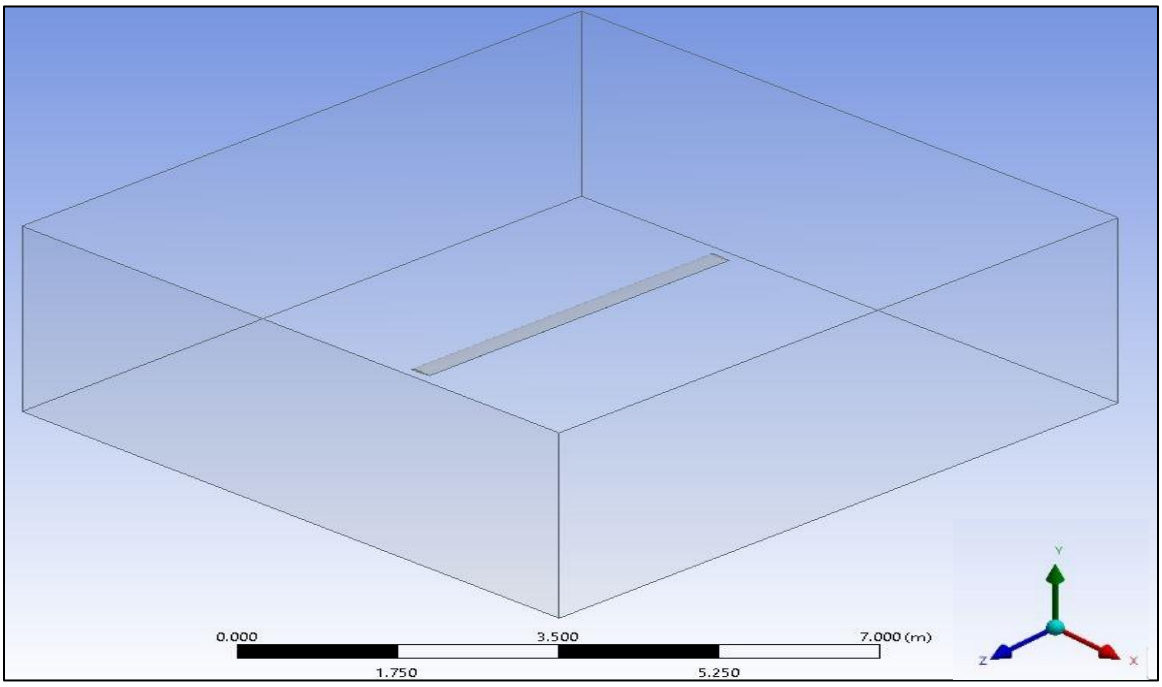


Fig. 2.5. 3-D Domain of the CFD model

For the analyses, 1,055,229 quadratic mesh elements, as shown in Fig. 2.6, are considered to obtain proper mesh convergence. The CFD formulation requires the specification of boundary conditions to state a well-posed mathematical problem. Four boundary conditions are specified on the fluid domain: inlet velocity, far-field velocity, outlet pressure, and symmetry velocity, and two boundary conditions are assigned on the mesh: fixed and symmetry deformations. There is no need to apply a wall boundary condition at the rotor blade cavity because the selection of the co-simulation interfaces automatically assigns this.

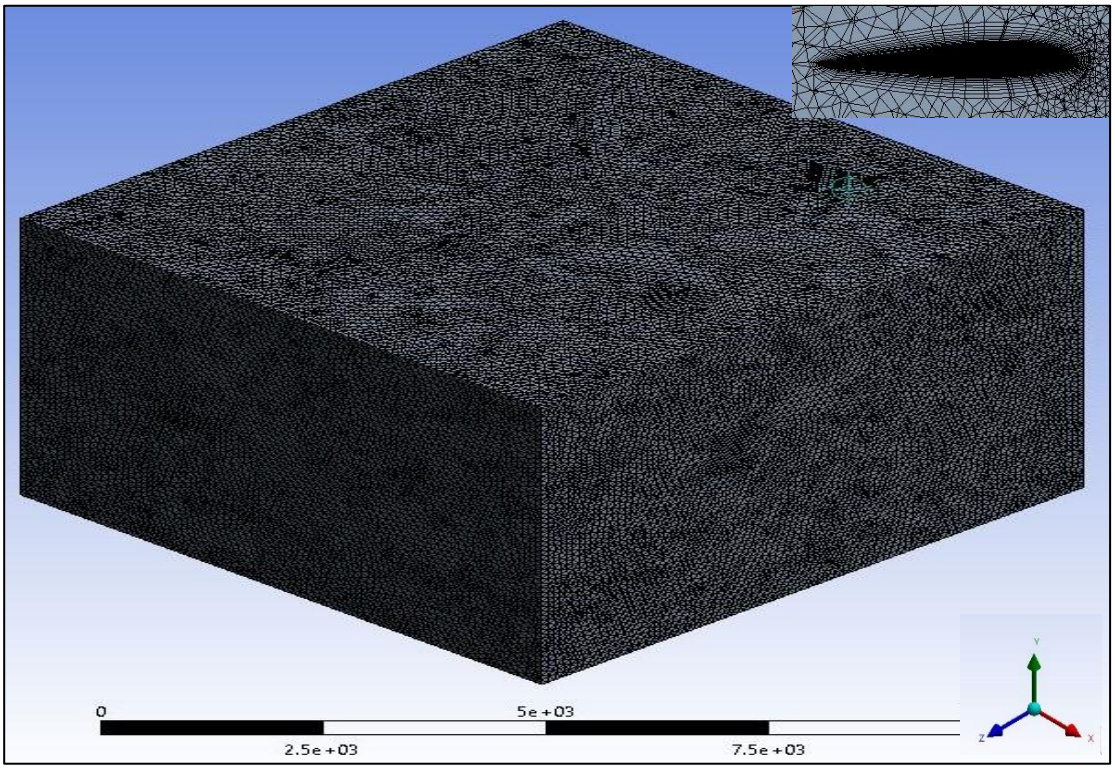


Fig. 2.6. CFD Mesh of the surrounding airflow domain

The boundary conditions must also represent the physics of the flow surrounding the rotor blade environment. For this purpose, an investigation of the Reynolds number is typically conducted to determine the physics of the flow and to determine the magnitude of the velocity

very far upstream of the rotor blade, also known as the freestream velocity. The range of velocities is different in the actual rotor blade operating in open space and the small-scale rotor blade in the wind tunnel and its capacity in the Aerodynamics Laboratory of the University of New Orleans. Therefore, two conditions are considered in CFD modeling the full-scale and small-scale rotor blades. The MBB Bo 105 operates at a cruise speed of 110 knots, equivalent to 204 km/h (56.67 m/s). Therefore, the boundary conditions are assigned to the full-scale rotor blade for different Reynolds numbers up to 1,019,068, equivalent to the cruise speed. There is a limitation of the experimental setup and velocity measurement in the lab; therefore, the small-scale rotor blades are operated up to 20 m/s in the wind tunnel, which is equivalent to generating Reynolds numbers up to 28,216. Different flow-speed and Reynolds number conditions are considered for the full-scale and small-scale rotor blades.

Table 2.3. Boundary conditions for the CFD model

| Boundary condition | Parameter |
|---|---|
| Steady inlet velocity in x-, y-, and z-directions | $V_x = V_\infty \cos\alpha$ m/s; $V_y = V_\infty \sin\alpha$ m/s; $V_z = 0$ m/s |
| Steady outlet pressure | $P = 0$ Pa |
| Steady far-field velocity in x-, y-, and z-direction | $V_x = V_\infty \cos\alpha$ m/s; $V_y = V_\infty \sin\alpha$ m/s; $V_z = 0$ m/s |
| Mesh fixed deformation in x-, y-, and z- | $U_x = 0$ m; $U_y = 0$ m; $U_z = 0$ m |
| Mesh symmetry deformation in x-direction | $U_x = 0$ m |

There are two conventions to represent velocity boundary conditions for an airfoil with different angles of attack. One is to rotate the airfoil with different angles of attack, and the other

is to consider components of velocity with angles of attack. The latter convention is adopted in this study due to the convenience of simulation. The boundary conditions of the CFD model are summarized in Table 2.3 and Fig. 2.7, respectively.

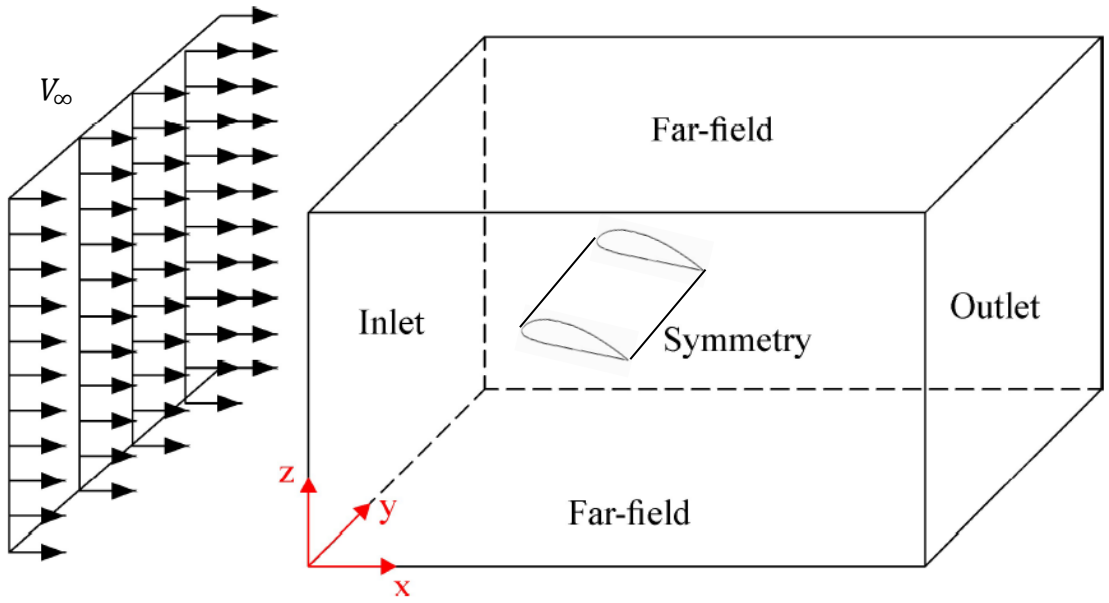


Fig. 2.7. Boundary conditions surfaces of the CFD domain. Description of the different faces of the CFD domain for the assignment of the boundary conditions.

The dynamic mesh model of Ansys Fluent is applied in this study to model the flow because the shape of the model changes with FSI coupling. The faces and interfaces are assigned with different dynamic mesh commands in the CFD domain. The inlet and outlet boundaries are assigned as deforming faces, the internal fluid cavity is defined as the system coupling face, and other faces are stationary in the dynamic mesh zones. Along with the usual conservation of mass and momentum of the fluid flow, the following transport equation applies according to dynamic mesh theory (Fluent, 2017)

$$\frac{d}{dt}\int_V \rho\phi dV + \int_{\partial V} \rho\phi(\vec{u}-\vec{u}_g).d\vec{A} = \int_{\partial V} \Gamma\nabla\phi.d\vec{A} + \int_V S_\phi dV \quad (1)$$

where $\rho$ is the fluid density, $\vec{u}$ is the flow velocity vector, $\vec{u}_g$ is the mesh velocity of the moving mesh, $\Gamma$ is the diffusion coefficient, and $S_\phi$ is the source term of $\phi$. Here $\partial V$ is used to represent the boundary of the control volume $V$.

### 2.4.3 Fluid-structure interaction model

The FSI represents a class of multi-physics analysis where the fluid flow affects the solid structures, affecting the fluid flow. The structural and fluid flow equations are solved independently from respective FE and CFD solvers. Then they are coupled through a system coupling solver for the FSI analysis, where interfacial loads and boundary conditions are exchanged after a converged increment. The necessary data, including displacements and forces, are transferred in the coupled solver from the solid model to the fluid model and vice versa for the FSI analysis.

## 2.5 Experimental Analysis

At first, a small-scale rotor blade is modeled and manufactured, and then two types of experimental arrangements, i.e., wind tunnel and vibration testing setups, are used in this study to validate the computational analysis of the aerodynamics and vibration characteristics.

### 2.5.1 Small-Scale Rotor Blade

The Parametric model of a small-scale blade of the Bo 105 helicopter rotor is generated using the SolidWorks 2020 software. The small-scale CAD model is then used in the Stratasys F170 3-D printer for manufacturing the model using the fused deposition modeling (FDM) method. The material used for the 3-D printed small-scale blade is the ABS (Acrylonitrile

butadiene styrene)-M30TM. The material properties of the manufactured small-scale model, i.e., ABS-M30TM, are depicted in Table 2.2.

### 2.5.2 Vibration Experiment

A vibration testing arrangement is used for experimental validation of the modal analysis with the small-scale rotor blade. There are two different arrangements that work together, i.e., a shaker arrangement to generate a regulated vibration on the specimen and a digital image correlation (DIC) system to capture images of the vibrating specimen for further analysis to get modal characteristics. The shaker arrangement consists of a GW-V20 PA100E signal force V20 shaker system, a 4-Channel SignalStar vibration controller, a 100 W voltage amplifier, and a 3055B5 accelerometer. The DIC system consists of two FASTCAM MC2.1 high-speed cube cameras. The vibration testing arrangement is shown in Fig. 2.8.

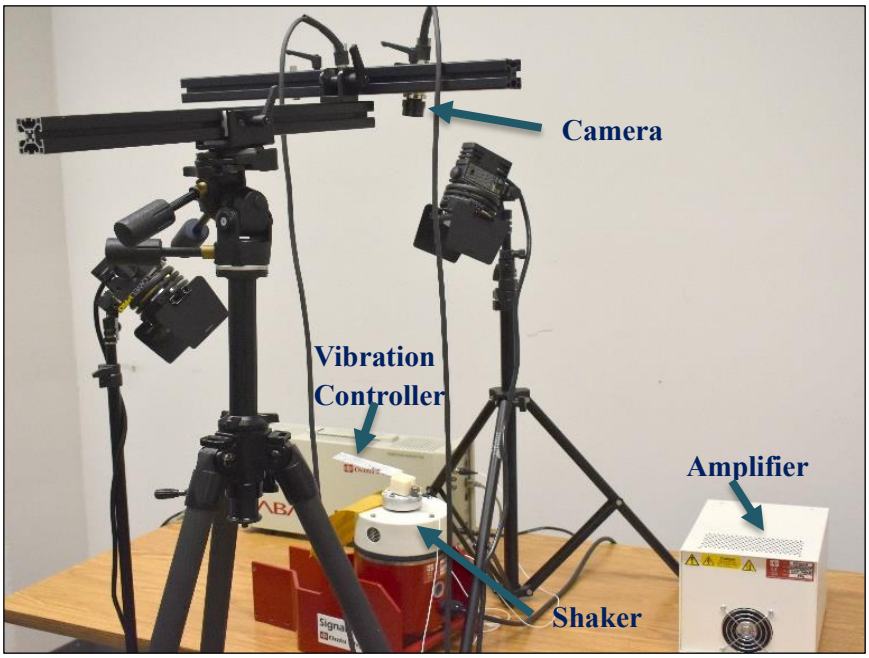


Fig. 2.8. Vibration experimental setup

The specimen is oscillated by a closed-loop system, where the shaker gets the signal from the vibration controller through the amplifier. The excitation signal on the shaker is monitored by the accelerometer, and it gives feedback to the controller. A close view of the small-scale rotor blade in the shaker is shown in Fig 2.9.

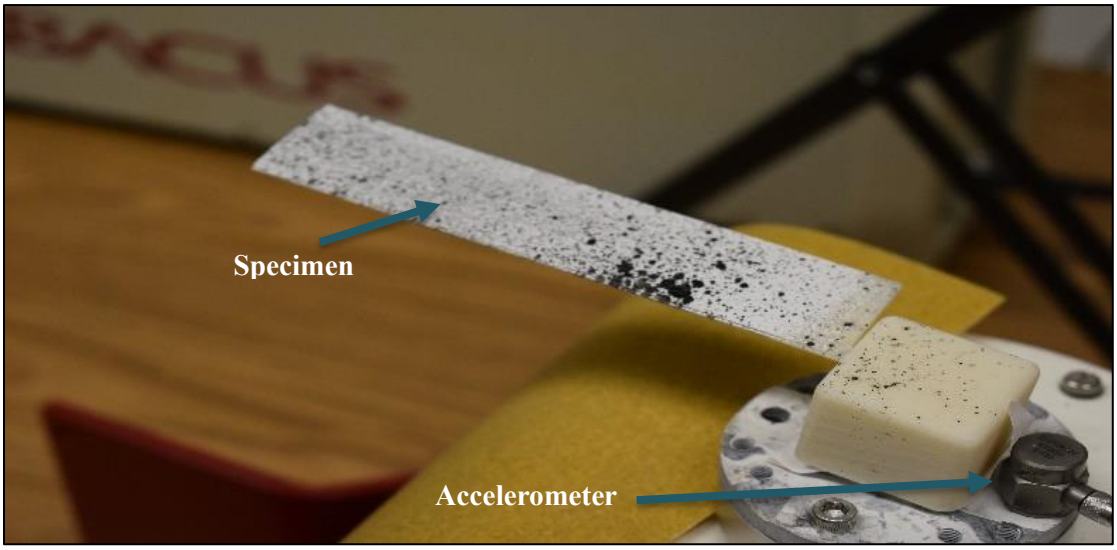


Fig. 2.9. Close view of the small-scale rotor blade attached to the shaker

The specimen is painted in white color, and then black dots are created using spray paint. The two high-speed cube cameras capture images during the vibration of the specimen with the regulation through VIC-snap software. Out-of-plane displacement is measured from the captured images using the VIC-3D software, and finally, the natural frequencies are obtained by the fast Fourier transform (FFT) of the displacement data. The natural frequencies of the specimen appear as high-amplitude data in the frequency domain.

### 2.5.3 Aerodynamic Experiment

A FLOTEK 1440 wind tunnel is used for the aerodynamic experimental validation of this study. In the wind tunnel, the air is drawn through the entrance cone into the test section by a

variable speed fan. A plastic honeycomb flow straightener with a length-to-diameter ratio of 10:1, assures a laminar airflow through the test section. The entrance cone has a contraction ratio of 12:1. The wind tunnel with the attached small-scale rotor blade is shown in Fig. 2.10.


Fig. 2.10. Wind tunnel experimental setup

A model positioning system along with a 3/8 EWT pistol grip sting balance from Aerolab is inserted into the test section of the wind tunnel. The sting balance works to measure the aerodynamic forces generated on the specimen, whereas the model positioning system holds the sting balance and specimen and regulates the angle of attack. An extended view of the test section of the wind tunnel and the small-scale rotor blade attached to the sting balance within the test section is shown in Fig. 2.11.

Fig. 2.11. A close view of the test section of the wind-tunnel and small-scale rotor blade attached to the sting balance

An air velocity transducer Model 8475 from TSI Inc. is used to measure the freestream velocity inside the wind-tunnel. Necessary fixtures to hold the specimen and the air velocity transducer are manufactured by using a Stratasys F170 3-D printer where the materials used is ABS-M30TM.

### 2.5.4 Sensitivity study of the experimental arrangement

Due to the limitations of experimental arrangement, especially the size of the wind tunnel cavity, the capacity of 3-D printing specimen, and the sensitivity of the data acquisition system available in the aerodynamics lab of the University of New Orleans, there is a shortcoming in the

experimental validation. The small-scale model tested in this study for experimental validation is of a different aspect ratio than the full-scale wing, which is a deviation from the similitude concept in terms of geometric similarity. Therefore, to further understand how it would work if the geometric similarity was attained in scaling the model, another small-scale model of the same aspect ratio of the rotor blade is investigated computationally through FE and FSI models. A dimensional comparison of the small-scale model in the experiment of this study and the similar geometric model of the full-scale rotor blade is depicted in Table 2.4.

Table 2.4. Comparison of parameters of the small-scale models

| Parameters | Small-scale model in experiment | Geometric similar to the rotor blade |
|---|---|---|
| Airfoil | NACA 23012 | |
| Length of the rotor blade, $l$ (cm) | 12.05 | 44.56 |
| Chord length of the airfoil, $c$ (cm) | 2.61 | 2.61 |
| Materials considered | 3D Printed ABS Plastic | |

Different computational models are developed with both geometric shapes, and those results in terms of natural frequencies, mode shapes, and aerodynamic coefficients are compared to understand the trend of output and validate the results.

The blade dynamics, when installed in the wind tunnel, do not have a fixed cantilever condition. Therefore, a shake test of the installed wing on the sting balance is conducted along with a sensitivity study using simulation package software for a similar arrangement to analyze the test installation impact on wing frequencies. The arrangement of the shake test of the installed wing mounted to the sting balance is shown in Fig. 2.12.

Fig. 2.12. The small-scale rotor blade connected to the sting balance which is attached to the shaker

A similar setup geometry modeled using SolidWorks 2020 software as shown in Fig. 2.13 and analyzed in Ansys Workbench 2019 R3.

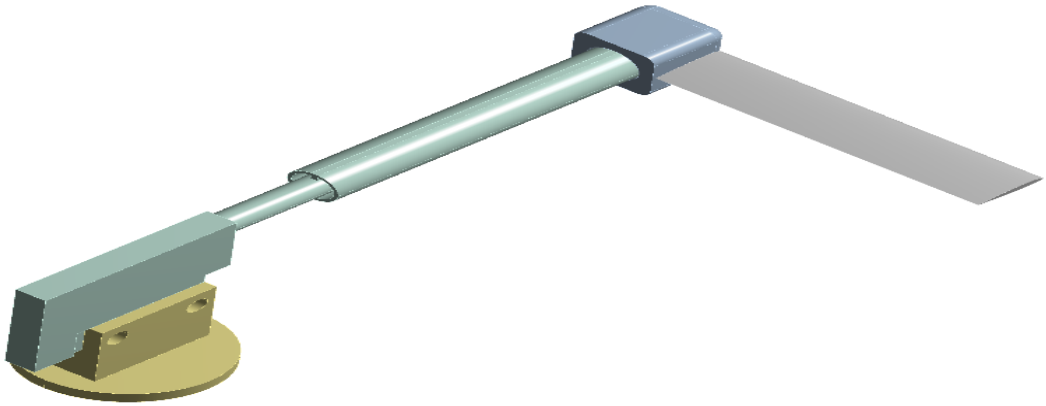

Fig. 2.13. FE model of the small-scale rotor blade attached to the sting balance

# CHAPTER 3

## The Wake and Vortex Formation

Advancement in helicopter aerodynamic research combines the findings in analytical solution, experimental results and empirical formulation, and numerical models. The complex flow field near a rotor blade makes the analytical solution challenging. Therefore, researchers are more inclined to investigate the numerical ways of solution possibilities and regain confidence in those numerical solutions using experimental validation. A flying machine conducts different functions using aerodynamic capabilities such as generating vertical lift in opposition to the weight of the flying machine, horizontal propulsion for forward movements, and a means to generate moment and forces to control the altitude and position of the flying machine in a three-dimensional space. In contrast to fixed-wing aircraft, which have different aerodynamic surfaces for different purposes, helicopters primarily depend on the rotor blade. Therefore, to meet the demanding roles of the helicopter rotor blade, a blade designer needs to explore and investigate the aerodynamic forces involved in a rotor blade operation.

A rotor blade's lifting ability depends on the local angles of attack and the local dynamic pressure. The different positions of the rotor blade are indicated using azimuth angle, which is defined as zero when the flow is downstream. As a spinning object, the rotor blade tip obtains the maximum speed, and for a constant blade AoA, the average rotor thrust depends on the square of the rotor blade rip speed (Leishman, 2006). The free stream velocity is an additional consideration for the forward flights in comparison to the hovering conditions. The effects of rotor wake are an essential element of predicting and understanding rotor blade load and other aerodynamic parameters. The rotor wake is dependent on the flying conditions and operating

states. The helical trajectories of blade tip vortices in the case of hovering flight are the simplest of operating states, whereas the rotor wake is skewed back in forward flight. In forward flight, the mutual proximity of different vortex filaments causes vortex-vortex interactions and complicated scenarios in wake topology.

The detail of wake flow is challenging to obtain experimentally because of its extensive 3-D nature and sensitivity to the geometric and operational parameters. Among other researchers, Vouros et al. (2021) investigated the impact of uncertainty in wake aerodynamic modeling on the robustness of helicopter rotor aeroacoustics analysis. The experimental data and empirical formulations based on the experimental results are used in this study to make a bridge between the computational outcome and empirical findings considering the challenges involved in the analytical solutions,

### 3.1 Structure of the Vortices

The fundamental wake model consists of three components—a concentrated tip vortex line, an inboard trailing vortex sheet, and a shed vortex, as shown in Fig. 3.1. Most of the trailing vortices outboard of the blade quickly roll up into concentrated tip vortices. The rest of the trailing wake and shed wake do not roll up until they are far downstream of the flow field. According to the conservation of circulation, the circulation gradients on a helicopter rotor blade determine the vorticity shed at specific spanwise locations behind the blade. The spanwise variations in the circulation generate trailing vorticity with the direction parallel to the local flow velocity. On the other hand, due to the transient periodical nature of the rotor blade's flow field, azimuthal variations produce shed vorticity radially oriented.

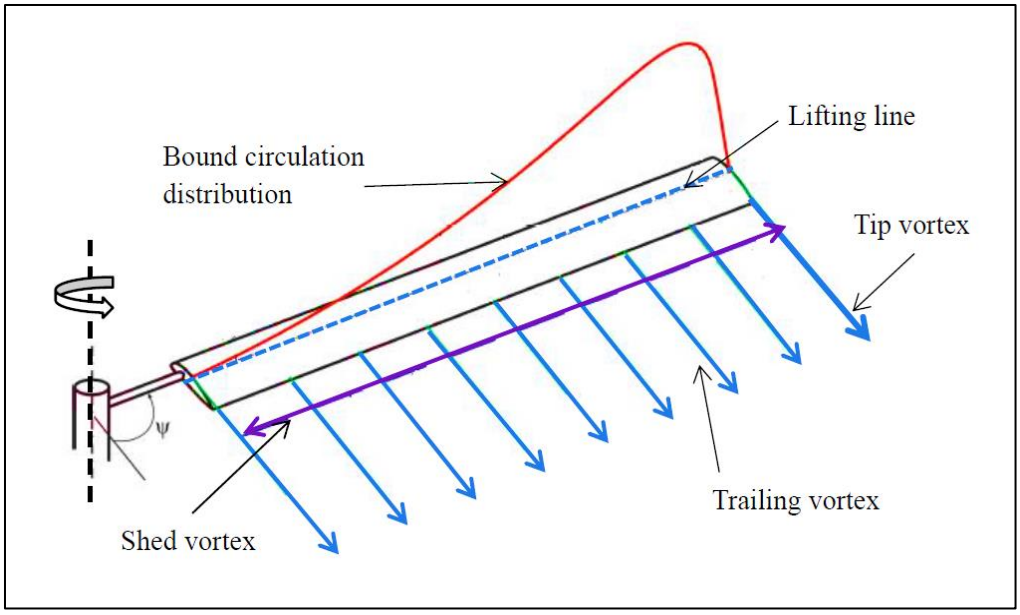


Fig. 3.1. Wake vorticity formation in a rotor blade with multiple vortex lines and bound circulation

### 3.1.1 Tip Vortex Models

The rapid drop in circulation near the blade tip causes a concentrated tip vortex. Blade-tip vortices influence the performances of a rotor by inducing drag and are still a challenging phenomenon to analyze for helicopter aerodynamics. The pressure difference between the lower and upper surface causes the vortex formation and drives the flow from the pressure side to the suction side around the tip (Goerttler et al., 2018). The blade tip's maximum lift value is found due to the rolled-up tip vortices. Tip vortices are also the primary source of harmonic airload. The Rankine vortex model (Leishman, 2006) is the simplest model of a vortex with a finite core where the swirl velocity is given by

$$V_\theta(\bar{r}) = \begin{cases} \left(\frac{\Gamma_v}{2\pi r_c}\right)\bar{r}, & 0 \le \bar{r} \le 1 \\ \left(\frac{\Gamma_v}{2\pi r_c}\right)\frac{1}{\bar{r}}, & \bar{r} > 1 \end{cases} \quad (1)$$

where, the core radius, $r_c$ is defined as the distance from the core center where the maximum tangential velocity is observed.

The Rankine vortex model has some limitations. The observed unrealistic higher swirl velocity, the vorticity, and the circulation values in the Rankine vortex model are different from that noticed in practice. To avoid the limitations, an alternate vortex model, i.e., The Lamb-Oseen model is considered for solving the simplified form of the Navier-Stokes formulation (Leishman, 2006). The Lamb-Oseen model for the swirl velocity is

$$V_\theta(\bar{r}) = \frac{\Gamma_v}{2\pi r_c \bar{r}}\left(1 - e^{-\alpha \bar{r}^2}\right) \tag{2}$$

where $\alpha = 1.25643$.

A further generalized series of desingularized velocity profiles is obtained in Vatistas model (Vatistas, 1991) where the swirl or tangential velocity can be expressed as

$$V_\theta(\bar{r}) = \left(\frac{\Gamma_v}{2\pi r_c}\right)\frac{\bar{r}}{(1 + \bar{r}^{2n})^{\frac{1}{n}}} \tag{3}$$

where n is an integer. For the n=1 vortex, which is commonly known as Scully vortex (Leishman, 2006)

$$V_\theta(\bar{r}) = \left(\frac{\Gamma_v}{2\pi r_c}\right)\frac{\bar{r}}{(1 + \bar{r}^{2})} \tag{4}$$

And for $n = 2$ vortex

$$V_\theta(\bar{r}) = \left(\frac{\Gamma_v}{2\pi r_c}\right)\frac{\bar{r}}{\sqrt{1 + \bar{r}^{4}}} \tag{5}$$

To obtain the formulation for axial velocity, and radial velocity, the governing Navier-Stokes equations in cylindrical coordinates for incompressible flow are written for the continuity as

$$\frac{1}{r}\frac{\partial}{\partial r}(rV_r) + \frac{\partial V_z}{\partial z} = 0 \tag{6}$$

where $\theta$ momentum:

$$V_r\frac{\partial V_\theta}{\partial r} + V_z\frac{\partial V_\theta}{\partial z} + \frac{V_r V_\theta}{r} = 0 \tag{7}$$

Using the Eqs. (6) and (7), and considering similar assumptions to Vatistas swirl velocity model, the axial velocity is found to be

$$V_z = -\frac{A}{z}\left\{1 - \frac{r^2}{(r_c^{2n} + r^{2n})^{\frac{1}{n}}}\right\} \tag{8}$$

And the radial velocity is found to be

$$V_r = -\frac{A}{2z^2}\left\{1 - \frac{r^2}{(r_c^{2n} + r^{2n})^{\frac{1}{n}}}\right\} \tag{9}$$

### 3.2 Vortex Model of the Rotor Wake

#### 3.2.1 Governing Equation of the Wake

3-D incompressible Navier-Stokes equations:

Eulerian frame of reference

$$\frac{\partial \omega}{\partial t} + (V.\nabla)\omega = (\omega.\nabla).V + \nu\Delta.\omega \tag{10}$$

Lagrangian frame of reference

$$\frac{D\vec{\omega}}{Dt} = (\vec{\omega}.\nabla)\vec{V} + \nu\Delta.\vec{\omega} \tag{11}$$

where the instantaneous value of vorticity, $\vec{\omega}$, and the local velocity field $\vec{V}$ is used in the equation to define the change of vorticity of a fluid element moving with the flow. The fundamental equation describing the transport of a point on the trailing vortex filament

$$\frac{d\vec{r}}{dt} = \vec{V}_{\mathrm{loc}}(\vec{r}, t), \vec{r}(t = 0) = \vec{r}_0, \tag{12}$$

where, $\vec{r} = \vec{r}(t) = \vec{r}(\psi_\omega, \psi_b)$ is a position vector at wake age $\psi_\omega$, and at an azimuth angle $\psi_b$.

The derivative on the left-hand side of Eq. 12 is expanded to give

$$\frac{d\vec{r}(\psi_b, \psi_\omega)}{dt} = \frac{\partial \vec{r}}{\partial \psi_\omega}\left(\frac{\partial \psi_\omega}{\partial t}\right) + \frac{\partial \vec{r}}{\partial \psi_b}\left(\frac{\partial \psi_b}{\partial t}\right) \tag{13}$$

The equation is simplified by the time derivatives

$$\frac{\partial \psi_\omega}{\partial t} = \frac{\partial \psi_b}{\partial t} = \Omega \tag{14}$$

The basic equation stating position in blade fixed coordinates

$$\frac{\partial \vec{r}}{\partial \psi_\omega} + \frac{\partial \vec{r}}{\partial \psi_b} = \frac{1}{\Omega}\,\vec{V}_{loc}\,(\vec{r}, t) \tag{15}$$

The partial differential equation governing the geometry of a single element of the vortex filament is

$$\frac{d\vec{r}(\psi_b,\psi_\omega)}{d\psi_b}+\frac{d\vec{r}(\psi_b,\psi_\omega)}{d\psi_\omega}=\frac{\vec{V}_\infty}{\Omega}+\frac{1}{\Omega}\sum_{j=1}^{N_v}\vec{V}_{\text{ind}}\left[\vec{r}(\psi_b,\psi_\omega),\vec{r}\left(\psi_j,\psi_\omega\right)\right] \tag{16}$$

Here the induced velocity can be determined using the Biot-Savart law

$$\vec{V}_{\text{ind}}\left[\vec{r}(\psi_b,\psi_\omega),\vec{r}\left(\psi_j,\psi_\omega\right)\right]\equiv\frac{1}{4\pi}\int\frac{\Gamma_v d\vec{\psi}_{\omega_j}\times\left(\vec{r}(\psi_b,\psi_\omega)-\vec{r}\left(\psi_j,\psi_\omega\right)\right)}{\left|\vec{r}(\psi_b,\psi_\omega)-\vec{r}\left(\psi_j,\psi_\omega\right)\right|^3} \tag{17}$$

### 3.2.2 Wake Model for Hovering Flight

The prescribed wake models suggest the locations of the rotor tip vortices as functions of wake age on the basis of experimental results.

#### 3.2.2.1 Landgrebe's Prescribed Wake Model (Leishman, 2006)

Based on several experiments conducted by Landgrebe with different combinations of variables including the number of blades, blade twist, rotor stability, and blade aspect ratio, the tip vortex geometry can be expressed by the equation

$$\frac{z_{tip}}{R}=\begin{cases}k_1\psi_w, & \text{for } 0\le\psi_w\le 2\pi/N_b\\ \left(\frac{z_{tip}}{R}\right)_{\psi_w=2\pi/N_b}+k_2\left(\psi_w-\frac{2\pi}{N_b}\right), & \text{for } \psi_w\ge 2\pi/N_b\end{cases} \tag{18}$$

and,

$$\frac{y_{tip}}{R}=r_{tip}=A+(1-A)\ exp\ (-\Lambda\psi_w\ ) \tag{19}$$

where, $\psi_w=2\pi/N_b$, and

$$k_1=-0.25\left(\frac{C_T}{\sigma}+0.001\theta_{tw}\right), \tag{20}$$

$$k_2=-(1.41+0.0141\theta_{tw})\sqrt{\frac{C_T}{2}}=-(1+0.01\theta_{tw})\sqrt{C_T} \tag{21}$$

where, $A = 0.78$ and $\Lambda = 0.145 + 27C_T$ are the empirically derived coefficients for the radial contraction and $z_{tip}/R$, and $y_{tip}/R$ denotes the vertical displacement and lateral displacements, respectively.

The outer end of the vortex sheet ($r = 1$) is represented by the equation

$$\left(\frac{z}{R}\right)_{r=1} = \begin{cases} K_{1,r=1}\psi_w, & \text{for } 0 \le \psi_w \le \dfrac{2\pi}{N_b} \\ K_{1,r=1}\psi_w\left(\dfrac{2\pi}{N_b}\right) + K_{2,r=1}\left(\psi_w - \dfrac{2\pi}{N_b}\right), & \text{for } \psi_w \ge \dfrac{2\pi}{N_b} \end{cases} \tag{22}$$

And the inner end of the vortex sheet ($r = 0$) is represented by the equation

$$\left(\frac{z}{R}\right)_{r=0} = \begin{cases} 0, & \text{for } 0 \le \psi_w \le \dfrac{2\pi}{N_b} \\ K_{2,r=0}\left(\dfrac{2\pi}{N_b}\right) + K_{2,r=1}\left(\psi_w - \dfrac{2\pi}{N_b}\right), & \text{for } \psi_w \ge \dfrac{2\pi}{N_b} \end{cases} \tag{23}$$

#### 3.2.2.2 Kocurek & Tangler's Prescribed Wake Model

Based on same set of generalized equation for tip vortex trajectories and another series of subscale rotor experiment conducted by Kocurek and Tangler, another prescribed model is formed. The generalized equation for $k_1$ is

$$k_1 = B + C\left(\frac{C_T^m}{N_b^n}\right) \tag{24}$$

where $B = -0.000729\theta_{tw}$, $C = -2.30206\theta_{tw}$, $m = 1.0 - 0.25e^{0.040\theta_{tw}}$ and $n = 0.5 - 0.0172\theta_{tw}$.

The equation for $k_2$ is

$$k_2 = -\left(C_T - C_{T_0}\right)^{1/2} \tag{25}$$

where $C_{T_0} = b^n(-B/C)^{1/\mathrm{m}}$ and $\lambda = 4.0\sqrt{C_T}$, with $A = 0.78$ is the regular contraction rate parameter.

### 3.2.3 Wake Models for Forward Flight

#### 3.2.3.1 Vortex Ring Model

Using a series of vortex ring or a vortex tube is a simple way to estimate the trailed wake vorticity in case of forward flight. An exact or analytic solution for induced velocity can be obtained using the vortex ring model, which is one of its major benefits. The induced velocity from one disingularized vortex ring of strength $\Gamma_v$ can be written as

$$V_z(r,z) = \frac{\Gamma_v}{4\pi}\int_{0+\delta\theta}^{2\pi-\delta\theta} \frac{z^2 + (R - rcos\theta)^2}{\sqrt{r_c^2\left(\sqrt{z^2} + (R - rcos\theta)^2\right)^2}} X \frac{R(R - rcos\theta)d\theta}{(R^2 - 2Rrcos\theta + z^2 + r^2)^{3/2}} \quad (26)$$

From this basic result of one ring, the net induced velocity at any point in the flow field can be obtained by summing the effects of all the rings representing the wake.

#### 3.2.3.2 Rigid or Undistorted Wake

The trailed vortices are represented by skewed helical filaments in the rigid or undistorted wake model. Fundamental equation describing transport of a point on trailing vortex filament

$$\frac{d\vec{r}}{dt} = \vec{V}_{\mathrm{loc}}(\vec{r},t), \vec{r}(t=0) = \vec{r}_0 \quad (27)$$

where, $\vec{r} = \vec{r}(t) = \vec{r}(\psi_\omega, \psi_b)$

An exact analytical solution may be obtained assuming a uniform streamwise velocity and a mean inflow, $\lambda_i =$ constant throughout the flow, i.e.,

$$\vec{V} = \Omega R\mu\hat{\imath} + \Omega R(\lambda_i)\hat{k} \tag{28}$$

Simplifying the governing equation by considering, $\frac{\partial\psi_\omega}{\partial t} = \frac{\partial\psi_b}{\partial t} = \Omega$

$$\frac{\partial\vec{r}}{\partial\psi_\omega} + \frac{\partial\vec{r}}{\partial\psi_b} = \frac{1}{\Omega}\vec{V}_{\text{loc}}(\vec{r}, t) \tag{29}$$

Under similar assumption, this can be written as

$$\frac{\partial\vec{r}}{\partial\psi_\omega} + \frac{\partial\vec{r}}{\partial\psi_b} = \mu\hat{\imath} + \lambda_i\hat{k} \tag{30}$$

where, $\psi_w$ is the wake age and $\psi_b$ is the azimuth angle at which vortex filament generate

Now, the required boundary conditions are

$$\psi_b: \vec{r}(\psi_b, \psi_w) = \vec{r}(\psi_b + 2\pi, \psi_w)$$

$$\psi_w: \vec{r}(\psi_b, 0) = r_v cos\psi_b\hat{\imath} + r_v sin\psi_b\hat{\jmath}$$

where, $r_v$ is the radial release point of the trail vortex filament from the blade

After simplification, the exact solution can be written as

$$\vec{r}(\psi_b, \psi_w) = (\mu\psi_w + r_v\cos(\psi_b - \psi_w))\hat{\imath} + r_v\sin(\psi_b - \psi_w)\,\hat{\jmath} + \lambda_i\psi_w\hat{k} \tag{31}$$

this is the undistorted or rigid vortex wake topology.

When $r_v = 1$, i.e., only tip vortices are assumed, the solution for tip vortex geometry

$$\frac{x_{tip}}{R} = x'_{tip} = \cos(\psi_b - \psi_w) + \mu\psi_w \tag{32}$$

$$\frac{y_{tip}}{R} = y'_{tip} = \sin(\psi_b - \psi_w) \tag{33}$$

$$\frac{z_{tip}}{R} = z'_{tip} = \lambda_i \psi_w = -\mu \psi_w tan\mathcal{X}_{TPP} \tag{34}$$

where the skew angle $\mathcal{X}_{TPP} = \tan^{-1}\left(-\frac{\lambda_i}{\mu}\right)$ and using momentum theory in forward flight

$$\lambda_i = \mu\, tan\alpha_{TPP} + \frac{kC_T}{2\sqrt{\mu^2 + \lambda_i^2}} \tag{35}$$

where $k$ is an induced power factor.

#### 3.2.3.3 Generalized Wake Model

Egolf and Landgrebe used a generalized wake model, where the vertical displacement of the tip vortices is

$$\frac{z_{tip}}{R} = z'_{tip} = -\lambda_i \psi_w - E\, G \tag{36}$$

where vertical displacement envelop function

$$E = \begin{cases} A_0 \psi_w \exp\,(A_1 \psi_w) & \text{for } \psi_w \leq 4\pi \\ M\psi_w + B & \text{for } \psi_w > 4\pi \end{cases} \tag{37}$$

Where the coefficients $A_0$, $A_1$, $M$, and $B$ are functions of the number of blades, the advance ratio, and the rotor thrust for a given factor. Here, the corresponding shape function

$$G = \begin{cases} \sum_{n=0}^{N} \{g'_{nc} \cos n(\psi_w - \psi_b) + g'_{ns} \sin n(\psi_w - \psi_b)\} \text{ for } 0 \leq \psi_w \leq 2\pi \\ \sum_{n=0}^{N} \{g''_{nc} \cos n(\psi_w - \psi_b) + g''_{ns} \sin n(\psi_w - \psi_b)\} \text{ for } \psi_w > 2\pi \end{cases} \quad (38)$$

### 3.2.3.4 Beddoes's Generalized Wake Model

Another parsimonious but very effective wake model is developed by Beddoes (Leishman, 2006). He suggested the following model

$$\lambda_i = \lambda_0(1 + Ex' - E|(y')^3|) \quad (39)$$

where $x' = x/R$ and $y' = y/R$

The region occupied by the wake at the rear of the disk

$$\lambda_i = 2\lambda_0 \left(1 - E \left|\left(y'_{tip}\right)^3\right|\right) \quad (40)$$

so that the vertical displacement of the tip vortex is given by

$$z'_{tip} = -\mu_z \psi_w + \int_0^{\psi_w} \lambda d\psi_b \quad (41)$$

where $z' = z/R$.

# CHAPTER 4

# Results and Discussion

## 4.1 Vibration Characteristics

### 4.1.1 Mesh Convergence of the FE Model

The Mesh convergence analysis for the finite element study is outlined in Fig. 4.1.

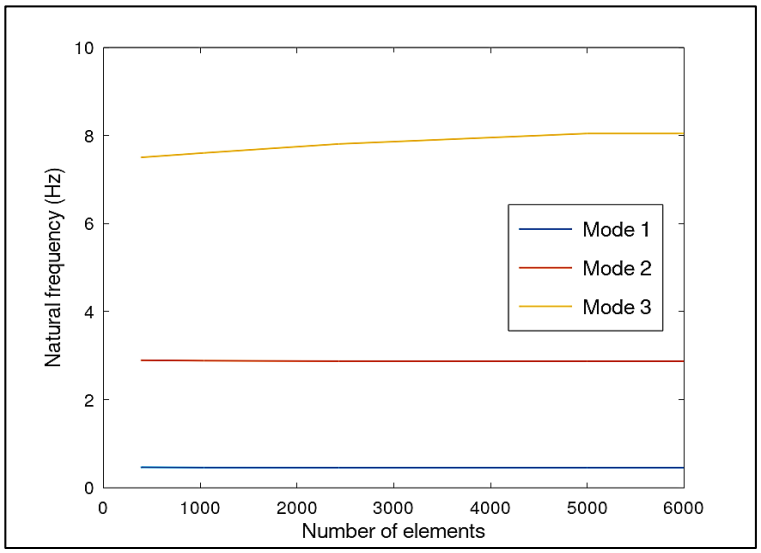


Fig. 4.1. Variation of the flapping natural frequencies of the full-scale Bo 105 rotor blade to the number of mesh elements

Figure 4.1 explains the variation of the fundamental natural frequencies of the triply coupled vibration of the rotor blade for the nonrotating case. The frequencies are obtained from the FE analysis in Ansys (Workbench, 2019) with the finest element size of 0.008 m. From Fig. 4.1, as the DOF increases, the trends of the natural frequencies become flattened after showing some initial changes indicating that the solution is already converged. The mesh convergence

study of the modal analysis shows that the natural frequencies remain the same for a number of mesh elements 5000 and above.

### 4.1.2 Validation of the Vibration by Experimental Results

The vibration characteristics, i.e., the natural frequencies and the mode shapes of the small-scale rotor blade, are obtained from the vibration experimental arrangement. A similar model is developed for the FE analysis and compared. The values of the natural frequencies obtained from the experimental and the FE analysis are shown in Table 4.1 with a comparison of their values. The mode shapes obtained from the experimental and FE analyses are shown in Fig. 4.2.

Table 4.1. Comparison of natural frequencies from the experimental data and the FE model for the small-scale rotor blade

| Mode | Natural Frequency (Hz) | | Percentage of deviation (%) |
|---|---|---|---|
| | Experimental results | FE results | |
| 1st Mode Flapping | 30.06 | 29.32 | 2.52 |
| 2nd Mode Flapping | 190.06 | 182.28 | 4.27 |
| 1st Mode Lead-lag | 219.03 | 231.30 | 5.20 |

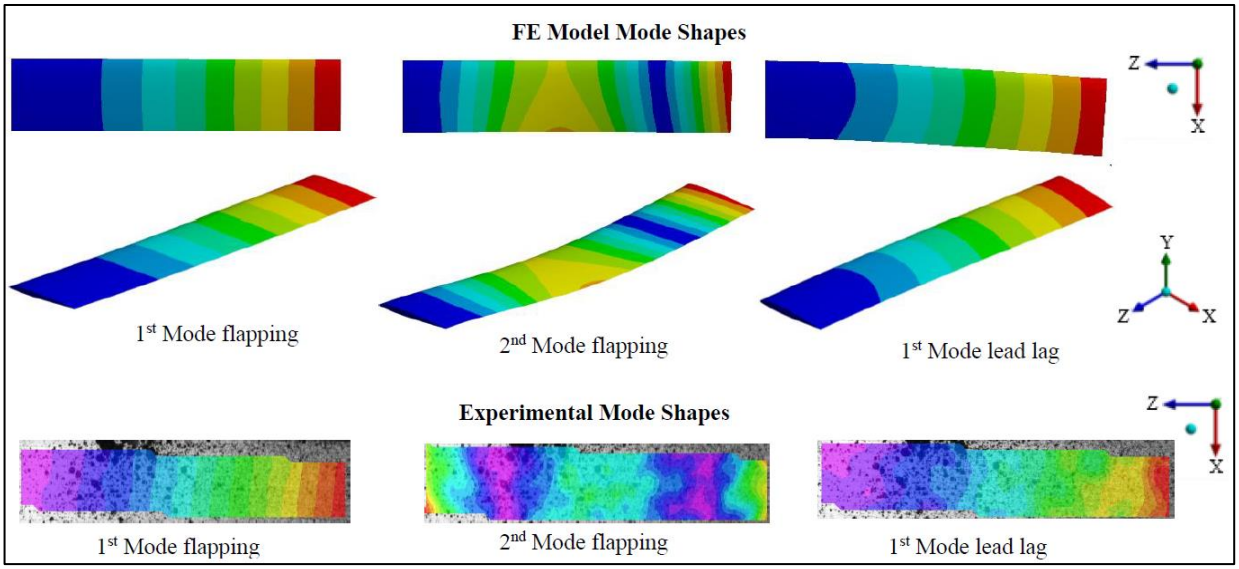


Fig. 4.2. Comparison of the mode shapes from the experiment and the FE model for the small-scale rotor blade attached to sting balance

The modal characteristics of the small-scale helicopter are calculated from the Fourier analysis of the time-varying out-of-plane deformation response to a random base excitation signal, as Pulok and Chakravarty (2022) outlined in their study. Random base excitation signals that the vibration controller controls go to the shaker, effectively exciting a broad bandwidth of frequencies simultaneously and providing sharp peaks on identifying the resonance frequencies. The small-scale rotor blade's first three natural frequencies and mode shapes are presented in Table 4.1 and Fig. 4.2, respectively. The experimental and FE model results show good agreements, validating the study. However, there is still a small percentage of difference, which is expected because of the surface finish, procedural variation of the 3-D printed specimen, and additional mass of the paint to create a speckle pattern for digital image correlation on the small-scale rotor blade.

### 4.1.3 Mode Shapes and Natural Frequencies of the Free Vibration

The natural frequencies and mode shapes of the full-scale Bo 105 rotor blade are computed for the nonrotating free vibration. The values of the natural frequencies for the free vibration are depicted in Table 4.2. In the table, the resonance frequencies of the first three modes in each type, i.e., flapping, lead-lag, and torsion, are listed.

Table 4.2. The natural frequencies of the full-scale nonrotating Bo 105 rotor blade

| Type of Vibration | Mode | Natural Frequency (Hz) |
|---|---|---|
| Flapping | 1st Mode | 0.6812 |
| | 2nd Mode | 4.2141 |
| | 3rd Mode | 11.666 |
| Lead-lag | 1st Mode | 4.5256 |
| | 2nd Mode | 28.004 |
| | 3rd Mode | 77.833 |
| Torsion | 1st Mode | 28.406 |
| | 2nd Mode | 85.304 |
| | 3rd Mode | 143.38 |

The mode shapes of the nonrotating free vibration analysis are found by the FE simulation and depicted in Fig. 4.3.

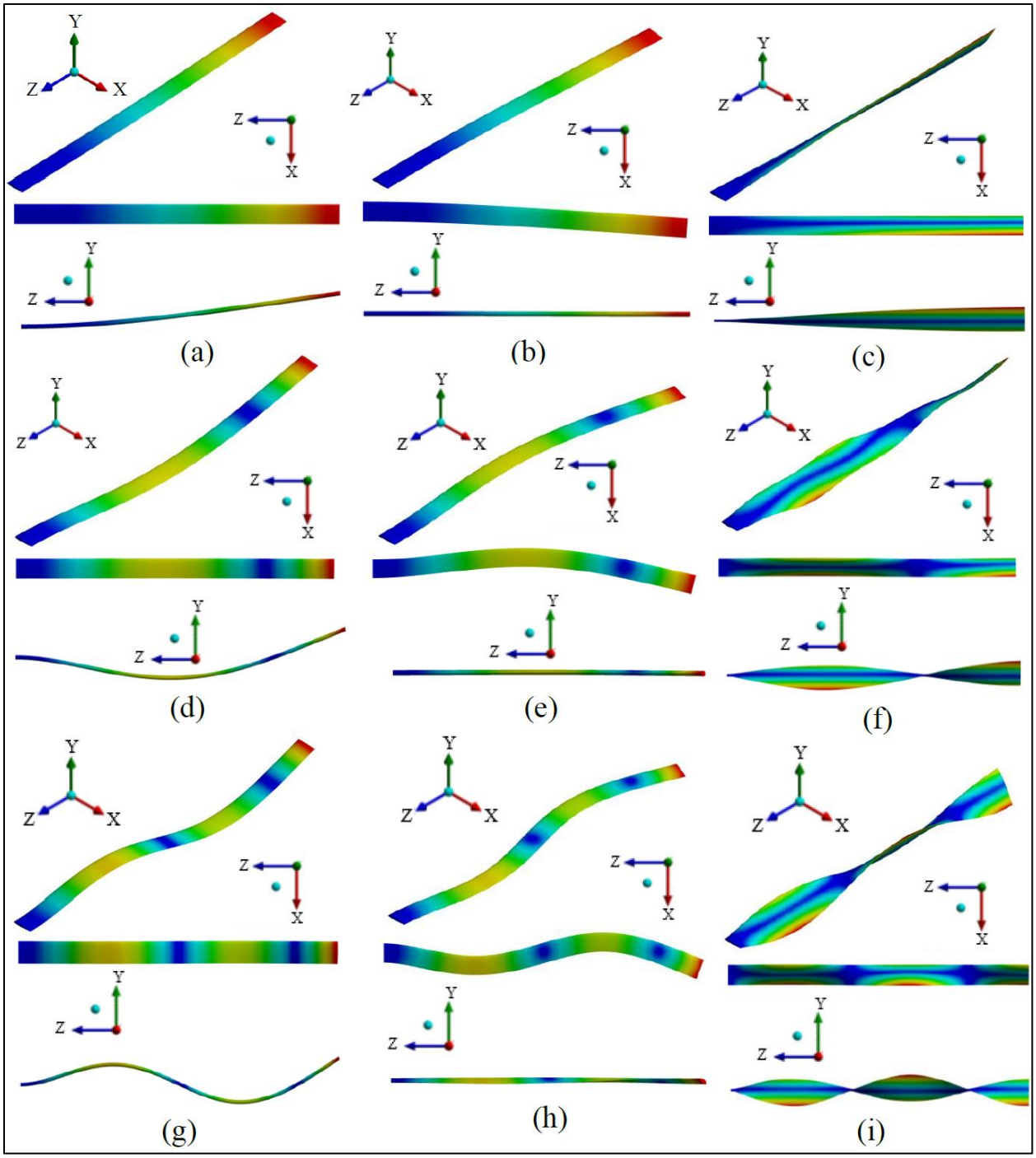


Fig. 4.3. Mode shapes of the nonrotating blade governed by (a) 1st mode flapping, (b) 1st mode lead-lag, (c) 1st mode torsion, (d) 2nd mode flapping, (e) 2nd mode lead-lag, (f) 2nd mode torsion, (g) 3rd mode flapping, (h) 3rd mode lead-lag, and (f) 3rd mode torsion

Figures 4.3(a)–(i) depict the mode shapes of the triply coupled vibration of the nonrotating helicopter rotor blade. The fundamental flapping and the lead-lag mode shapes are given in Figs. 4.3(a) and (b), respectively, while Fig. 4.3(c) shows the fundamental torsion governed mode having a blue axis running parallel to the elastic axis of the blade. This axis goes through the shear center, suggesting that the blade is about to rotate with respect to this axis. Figures 4.3(d)–(f) explain the similar phenomena for the second mode governed by the flapping, lead-lag, and torsion, respectively. Following this, Figs. 4.3(g)–(i) describe the third mode of the triply coupled vibration of the rotor blade. Although the coupling effect, as seen from the mode shapes, seems to be smaller, it can gradually become larger with higher modes. This seems possible from Figs. 4.3(g) and (f), where in the former, the torsional effect is obvious and, in the latter, the blue axis gets distorted due to the coupled effect. The values of lead-lag natural frequencies are higher than flapping natural frequencies, as shown in Table 4.2, which is expected because of the area moment of inertia about the flap-wise axis is smaller than the lead-lag axis for the airfoil cross-sections (White et al., 2011). Torsional natural frequencies are the maximum due to the torsional stiffness.

The resonance frequencies and mode shapes obtained in this study show a similar trend of results in comparison to what was observed in the literature. A comparison of the resonance frequencies is shown in Table 4.3.

Table 4.3. Comparison of the natural frequencies of the Bo 105 rotor blade

| Type of Vibration | Mode | Natural Frequency (Hz) | | | | | | |
|---|---|---|---|---|---|---|---|---|
| | | This Study | Sarker (2018) FE | Sarker (2018) Analyt. | Kim et al. (2013) | Sarker (2018) Analyt. | Johnson (1977) | Reddy and Ganguly (2003) |
| | | nonrotating | | | rotating | | | |
| Flapping | 1st Mode | 0.6812 | 0.65 | 0.69 | 6.03 | 7.76 | 1.12 | 1.146 |
| | 2nd Mode | 4.2141 | 4.04 | 4.33 | 14.71 | 18.53 | - | 3.511 |
| | 3rd Mode | 11.666 | 11.27 | 12.13 | 24.30 | 32.29 | - | 7.992 |
| Lead-lag | 1st Mode | 4.5256 | 4.61 | 4.74 | 4.07 | 5.65 | 0.74 | 0.744 |
| | 2nd Mode | 28.004 | 28.73 | 29.72 | 26.79 | 34.05 | - | 4.445 |
| | 3rd Mode | 77.833 | 79.48 | 83.22 | - | 88.16 | - | 11.309 |
| Torsion | 1st Mode | 28.406 | 31.36 | 29.37 | 23.13 | 29.37 | 3.66 | 4.551 |
| | 2nd Mode | 85.304 | 93.93 | 88.03 | - | 88.03 | - | 13.488 |
| | 3rd Mode | 143.38 | 157.10 | 146.60 | - | 146.62 | - | |

Among other researchers, Sarker (2018) performed the modal analysis of the Bo 105 rotor blade for free vibration, considering both rotating and nonrotating rotor blades. The difference between Sarker (2018) and this study is in the solution procedure. A finite element model is developed in this study, whereas Sarker (2018) considered the Method of Lines to obtain analytical resonance frequencies. For Bo 105 helicopter rotor blades, Johnson (1977), Reddy and Ganguly (2003), and Kim et al. (2013) stated fundamental resonance frequencies in rotating cases. The outcome of this study shows a similar result to that of nonrotating instances

from the literature. Various material compositions and different procedures were considered in determining resonance characteristics in the literature. In contrast, an experimentally validated FE model of the Bo 105 rotor blade is considered in this study. The mode shapes of the nonrotating free vibration analysis also show a similar phenomenon to that obtained from the literature (Sarker, 2018).

## 4.2 Aerodynamic Performances

### 4.2.1 Mesh Convergence of the CFD Model

The FSI simulation is operated for the different numbers of mesh elements of both the FE and CFD models to converge the results. The aerodynamic lift and drag coefficients are considered in the mesh convergence study for the CFD part of the FSI simulation and shown in Fig. 4.4. The simulation shows convergent results for more than 1,050,000 CFD mesh elements.

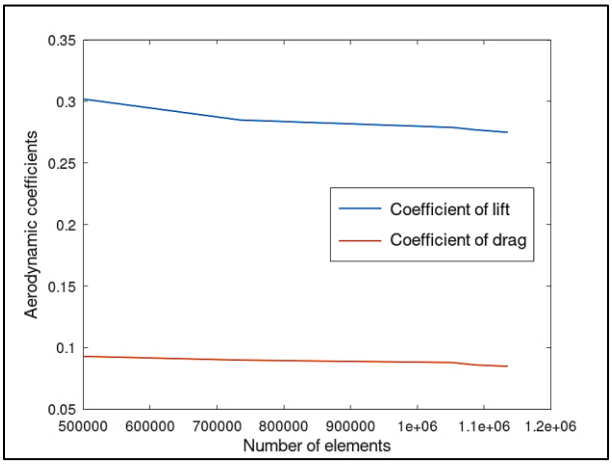


Fig. 4.4. Variation of the aerodynamic coefficients of the Bo 105 rotor blade to the number of mesh elements

### 4.2.2 Experimental Validation of FSI results

The aerodynamic characteristics of the numerical model are validated by comparing the aerodynamic coefficients with the wind tunnel experimental results for the small-scale rotor blade. The aerodynamic lift and drag coefficients with the angles of attack for the small-scale rotor blades are presented and compared in Figs. 4.5 and 4.6, respectively.

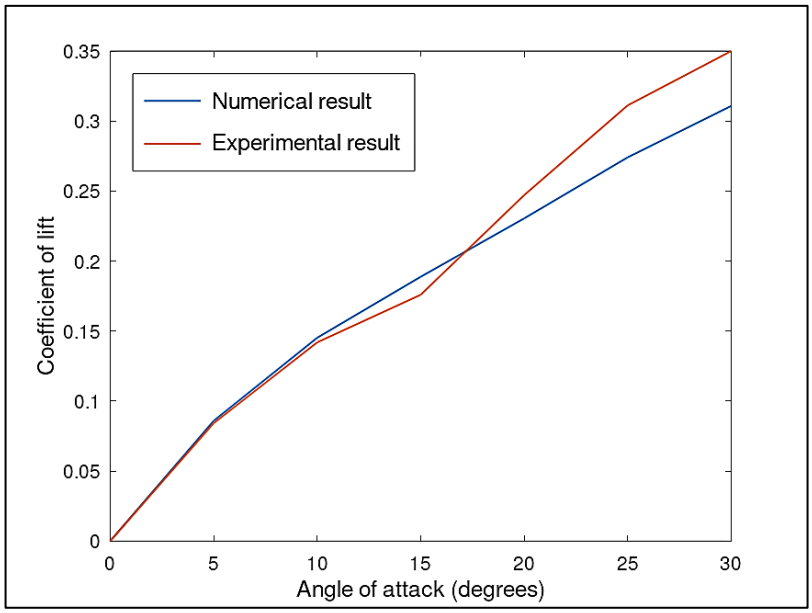


Fig. 4.5. Comparison of the coefficients of lift vs angle of attack for the small-scale rotor blade for Re = 28,216

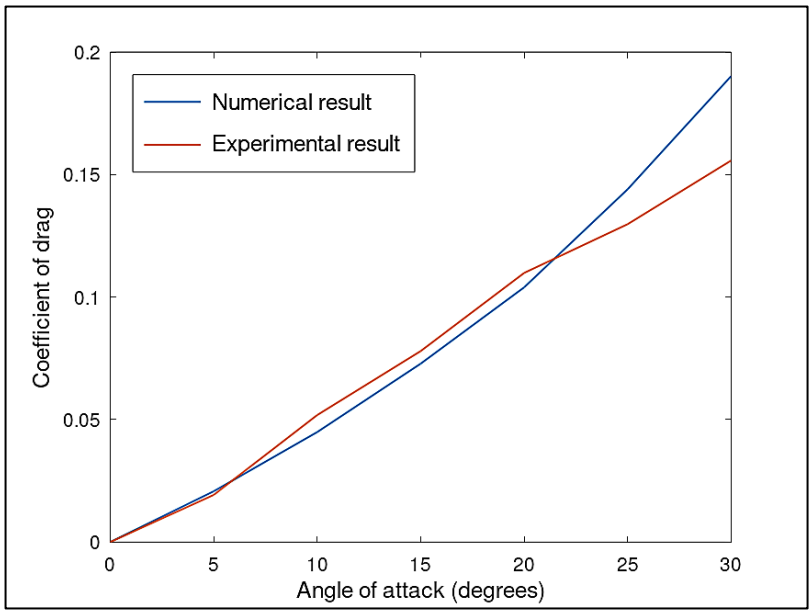


Fig. 4.6. Comparison of the coefficients of drag vs angle of attack for the small-scale rotor blade for Re = 28,216

The analysis shows that the experimental and computational FSI results are comparable for the small-scale model of the rotor blade in terms of aerodynamic coefficients of lift and drag. There are some variations in experimental and computational results. These variations might be due to the fixtures' additional surface area and mass to attach the specimen with the sting balance inside the wind tunnel.

### 4.2.3 Aerodynamic Results

Aerodynamic coefficients of lift and drag of the rotor blade are computed from the output of the FSI simulation. The coefficients of lift and drag, and lift-to-drag ratio are shown in Figs. 4.7, 4.8, and 4.9, respectively. Velocity and pressure contours for the full-scale Bo 105 rotor blade are shown in Fig. 4.10.

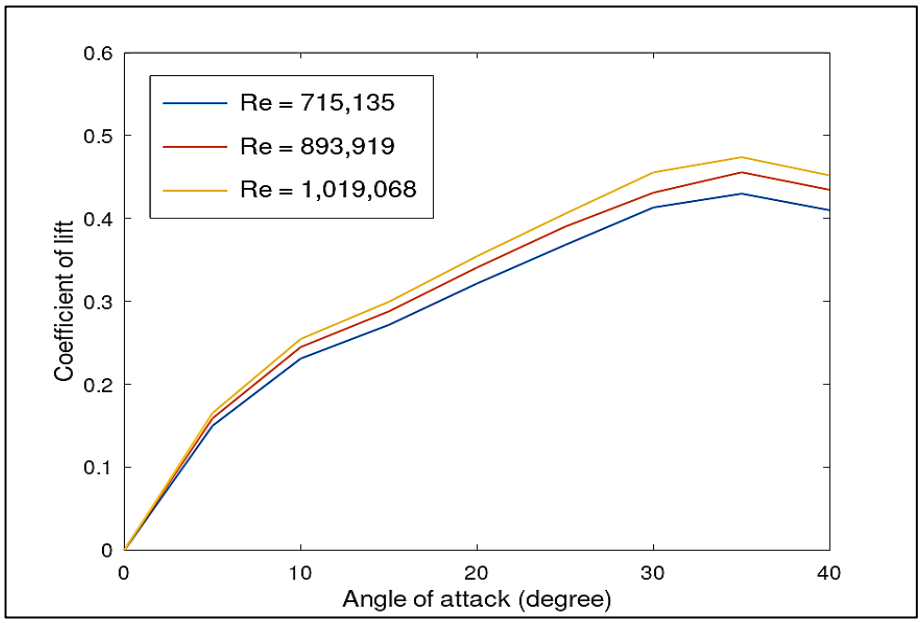


Fig. 4.7. The coefficient of lift vs angle of attack at different Reynolds numbers for the Bo 105 rotor blade

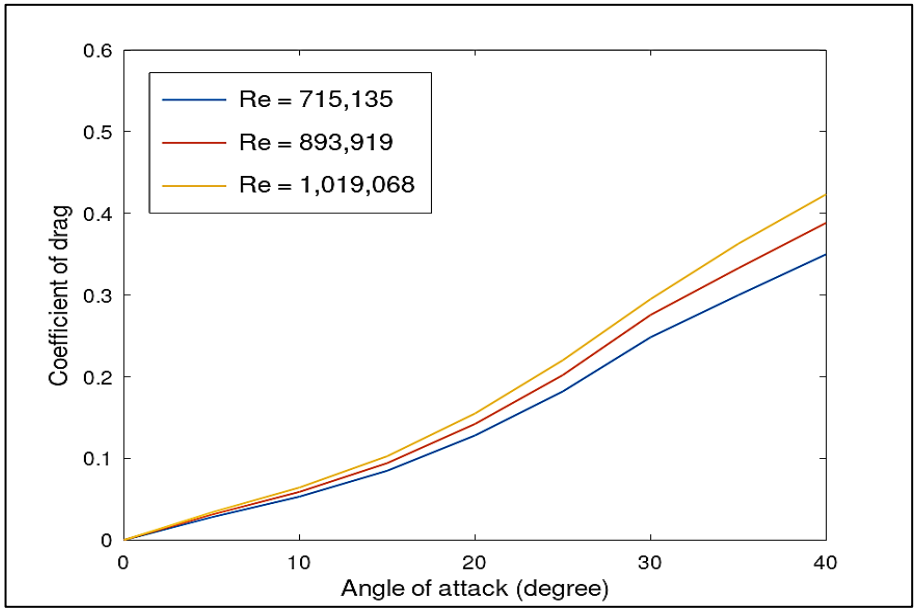


Fig. 4.8. The coefficient of drag vs angle of attack at different Reynolds numbers for the Bo 105 rotor blade

Figure 4.7 shows an increment of the coefficient of lift with the angle of attack, which is expected because a higher pressure difference between the upper and lower surfaces of the rotor blade is generated due to the increased angle of attack. The increment of coefficient of drag with the angle of attack, as found and shown in Fig. 4.8, is the effect of flow separation that generates the pressure drag at higher angles of attack.

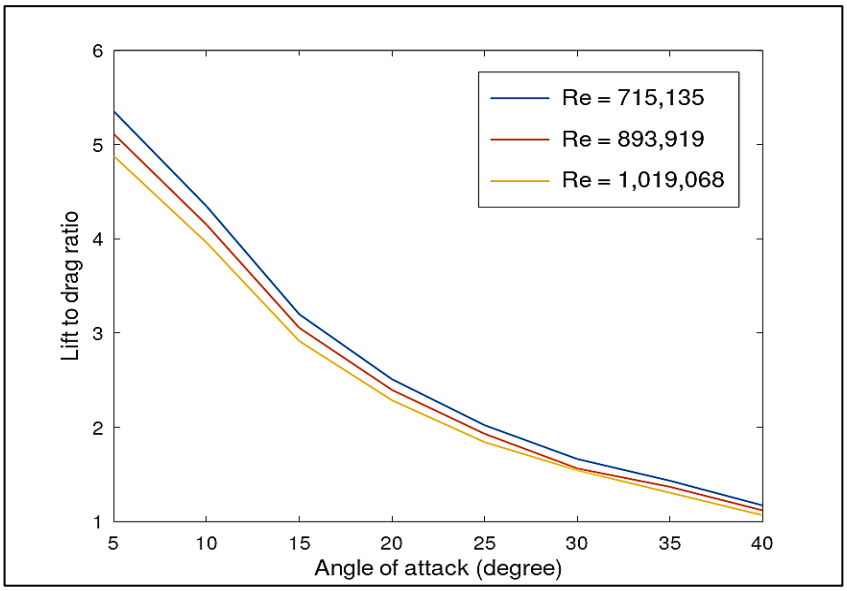


Fig. 4.9. The lift-to-drag ratio vs angle of attack at different Reynolds numbers for the Bo 105 rotor blade

The aerodynamic coefficients with the angles of attack for the full-scale rotor blade are presented and compared for different Reynolds numbers in Figs. 4.7–4.9. Fig. 4.7 shows an increment of the coefficient of lift with the angle of attack, which is expected because a higher pressure difference between the upper and lower surfaces of the rotor blade is generated due to the increased angle of attack. On the other hand, the increment of drag coefficient with the angle of attack, as found and shown in Fig. 4.8, is accounted for by the flow separation effects that generate the pressure drag at higher angles of attack.

The increment of pressure difference with increasing angle of attack is also observed in Fig. 4.10 from the pressure contour diagrams.

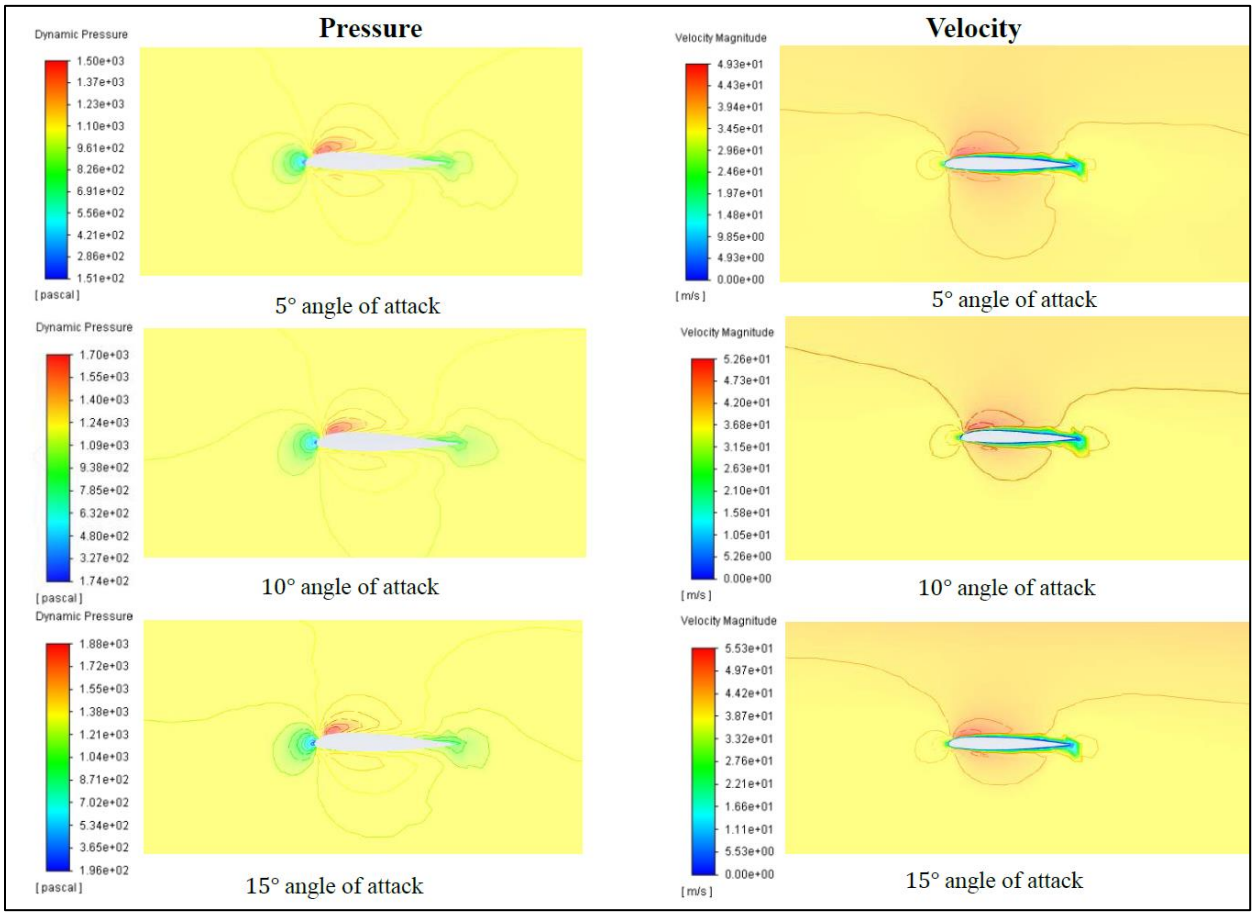


Fig. 4.10. The dynamic pressure and velocity magnitude contour plot in x-y plane for the Bo 105 rotor blade near the tip

### 4.3 Sensitivity Study of Experimental Validation

The small-scale rotor blade considered in this study for experimental validation is not complied with the geometric similarities in terms of similitude technique due to the limitations in the available experimental setup. Therefore, for further validation, another similar geometric model of a small-scale rotor blade with the same aspect ratio as the full-scale Bo 105 helicopter

rotor blade is considered for the computational study. Results of modal analysis using the FE model in natural frequencies and mode shapes are depicted in Table 4.4 and Fig. 4.11, respectively.

Table 4.4. The natural frequencies of the small-scale nonrotating Bo 105 rotor blade of same aspect ratio

| Type of Vibration | Mode | Natural Frequency (Hz) |
|---|---|---|
| Flapping | 1st Mode | 2.1256 |
| | 2nd Mode | 13.313 |
| | 3rd Mode | 37.247 |
| Lead-lag | 1st Mode | 17.229 |
| | 2nd Mode | 106.87 |
| | 3rd Mode | 294.51 |
| Torsion | 1st Mode | 82.164 |
| | 2nd Mode | 246.14 |
| | 3rd Mode | 411.13 |

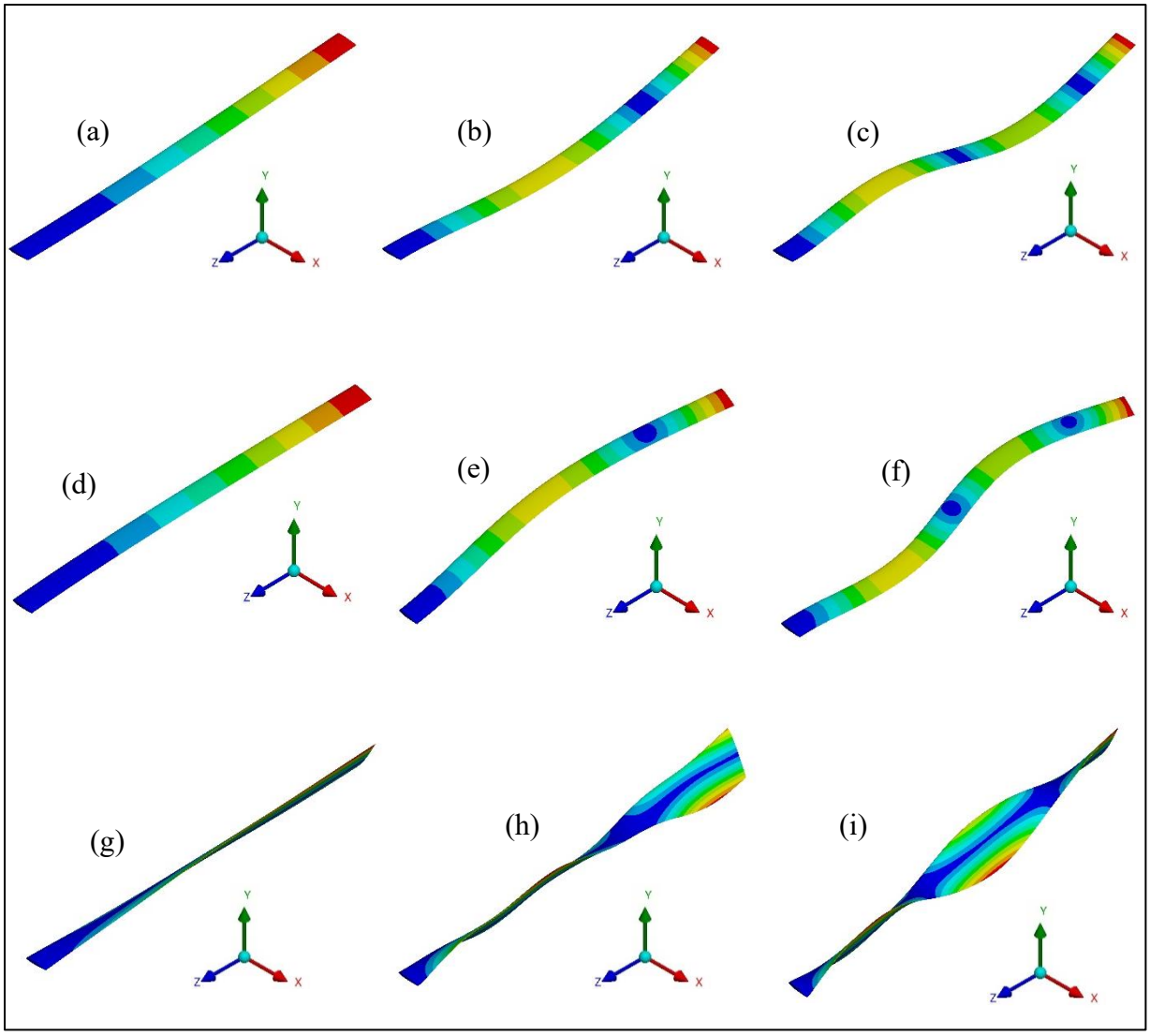


Fig. 4.11. Mode shapes of the nonrotating small-scale blade of same aspect ratio governed by (a) 1st mode flapping, (b) 1st mode lead-lag, (c) 1st mode torsion, (d) 2nd mode flapping, (e) 2nd mode lead-lag, (f) 2nd mode torsion, (g) 3rd mode flapping, (h) 3rd mode lead-lag, and (f) 3rd mode torsion

The aerodynamic coefficients of lift and drag are also obtained using the FSI model from both small-scale models. One is short-span due to experimental limitations, and another is full-span. The comparison of the coefficients of lift and drag with the angle of attack for the full-span and short-span small-scale rotor blade is depicted in Figs. 4.12 and 4.13, respectively.

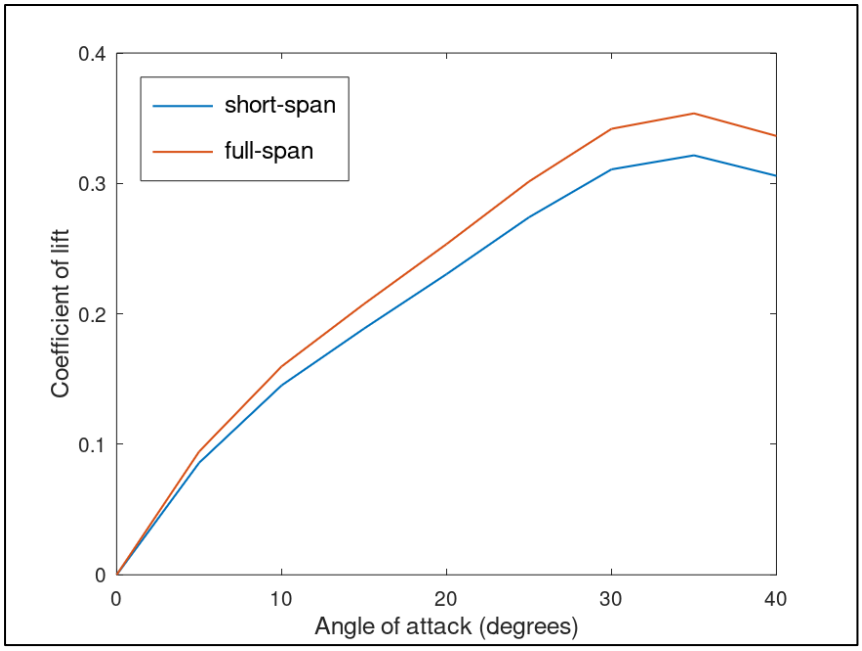


Fig. 4.12. Comparison of the coefficient of lift of the short-span and full-span small-scale rotor blades

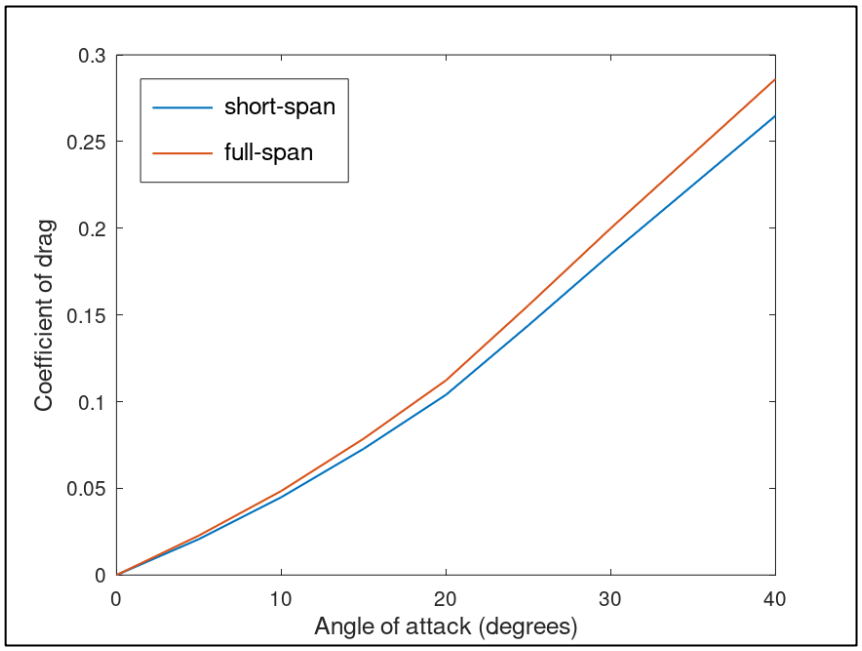


Fig. 4.13. Comparison of the coefficient of drag of the short-span and full-span small-scale rotor blades

The aerodynamic coefficient results from Figs. 4.12 and 4.13 show a similar trend for the full-span and short-span small-scale rotor blades. Therefore, support the feasibility of the experimental validation study.

When installed in the wind tunnel, the blade dynamics do not have a fixed cantilever condition. Therefore, a shake test of the installed wing on the sting is conducted along with a sensitivity study using simulation package software for a similar arrangement to analyze the test installation impact on wing frequencies. The natural frequency of the small-scale rotor blade when it is attached to the sting balance is shown in Table 4.5. The mode shapes for the small-scale rotor blade attached to the sting balance are shown in Fig. 4.14.

Table 4.5. Comparison of natural frequencies from the experimental data and the FE model for the small-scale rotor blade attached to the sting balance

| Mode | Natural Frequency (Hz) | | Percentage of deviation |
|---|---|---|---|
| | Experimental results | FE results | |
| 1st Mode Flapping | 28.48 | 28.71 | 0.81 |
| 2nd Mode Flapping | 192.23 | 197.12 | 2.54 |
| 1st Mode Lead-lag | 156.75 | 159.63 | 1.84 |

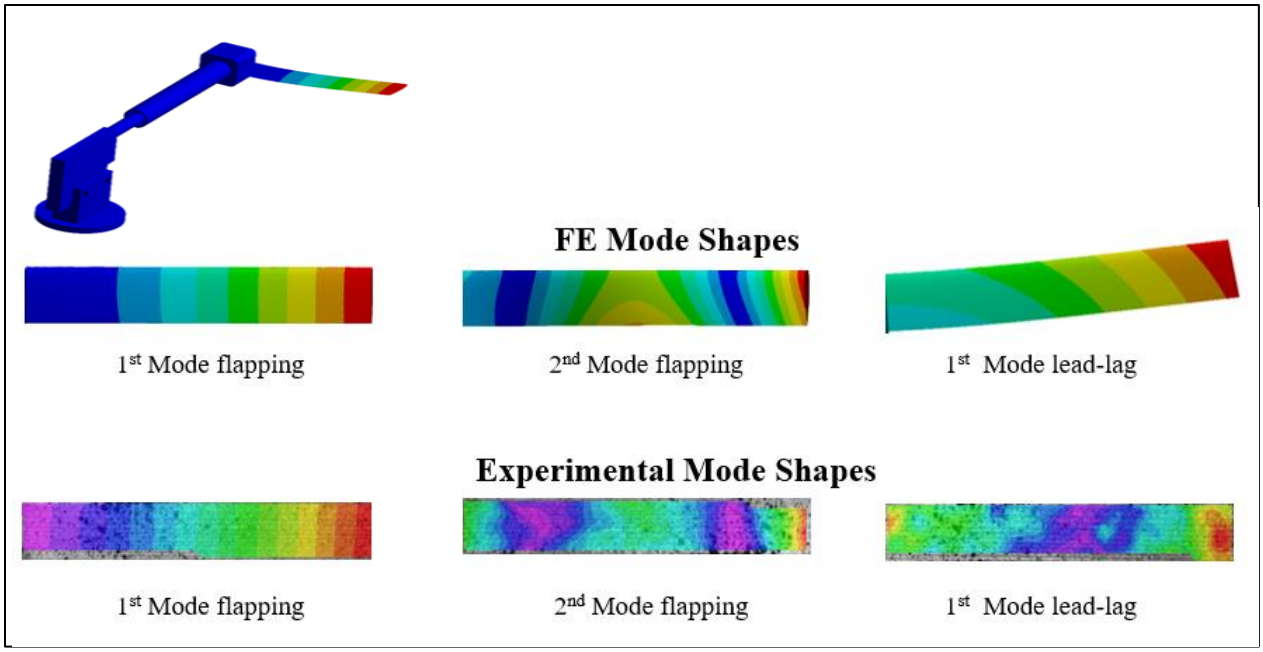


Fig. 4.14. Comparison of the mode shapes from the experiment and the FE model for the small-scale rotor blade attached to sting balance

Comparative natural frequencies of the small-scale rotor blade with and without attaching to sting balance are shown in Table 4.6.

Table 4.6. Comparison of natural frequencies from the experimental data and the FE model for the small-scale rotor blade attached to the sting balance

| Mode | Natural Frequency (Hz) | | Percentage of deviation |
|---|---|---|---|
| | Without Sting | With Sting | |
| 1st Mode Flapping | 29.32 | 28.48 | 2.86 |
| 2nd Mode Flapping | 182.28 | 192.23 | 5.46 |
| 1st Mode Lead-lag | 231.30 | 156.75 | 32.23 |

Comparative mode shapes of the small-scale rotor blade with and without attaching to the sting balance are depicted in Fig. 4.15.

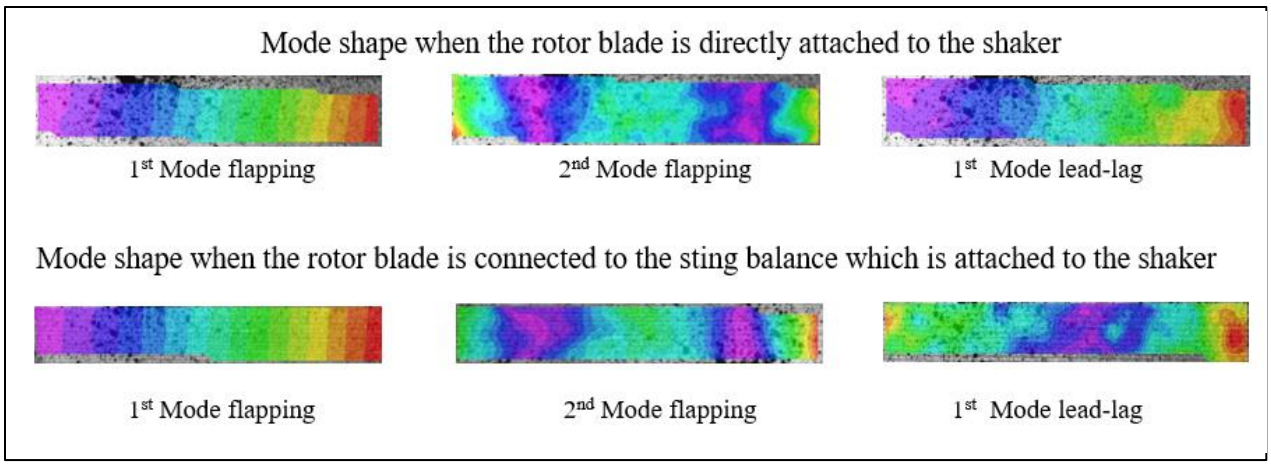


Fig. 4.15. Comparison of the mode shapes of the small-scale rotor blade with and without attaching to the sting balance.

## 4.4 Wake and Vortex Results

### 4.4.1 Structure of the Tip Vortices

The tangential or swirl velocity of a tip vortex with a finite core is obtained using Eqs. 1−3 which represents different vortex models. The tangential velocity $V_\theta$ is normalized by the strength over the vortex core perimeter $\Gamma/2\pi r_c$, and the distance from the vortex center is nondimensionalised by the vortex core radius. In addition, the constant for Lamb-Oseen model is considered $\alpha = 1.25643$ (Leishman, 2006). The tangential velocity profiles using different vortex models are shown in Fig. 4.16.

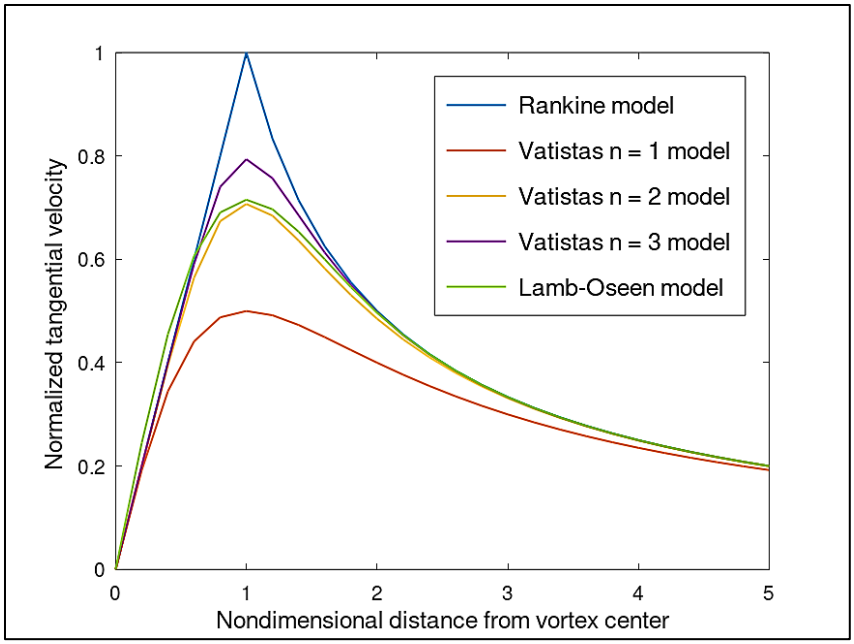


Fig. 4.16. The nondimensional tangential (swirl) velocity ($V_\theta/(\Gamma/2\pi r_c)$) profile of the 2-D vortex for different models

Tangential velocity increases till a peak value at the vortex core radius, i.e., $r = r_c$, and then gradually decreases with increasing the distance from the core as shown in Fig. 4.16. The Rankine model exhibits a significantly higher value of the tangential velocity at $r = r_c$ which is different from that observed in practice (Leishman, 2006).

Swirl and axial velocities using different models are calculated using Eqs. 2, 8, and 9 and plotted as shown in Figs. 4.17 and 4.18. The velocities are normalized by their peak values, i.e., the swirl velocity $V_\theta$ by $V_{\theta\,max}$, and the axial velocity $V_z$ by $V_{z\,max}$.

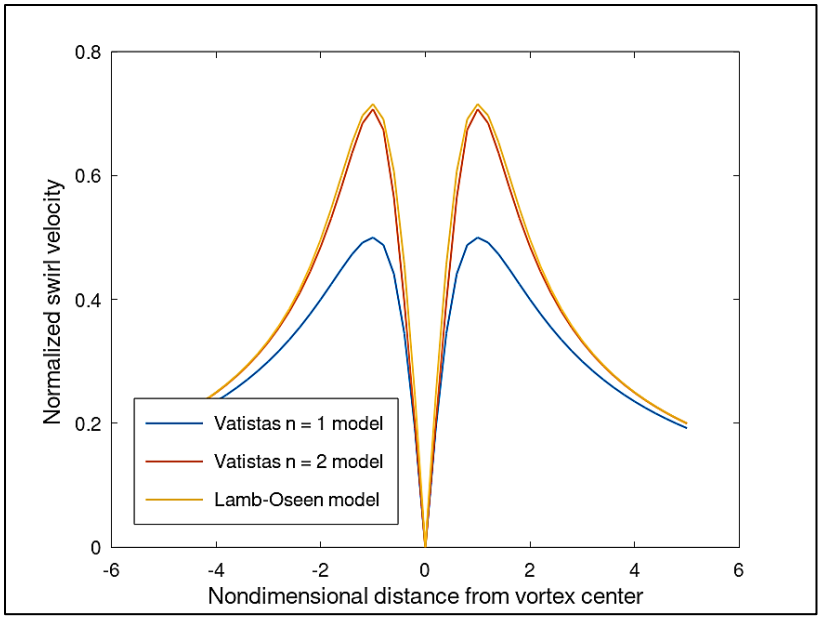


Fig. 4.17. The nondimensional swirl velocity ($V_\theta / V_{\theta\,max}$) profile for different vortex models

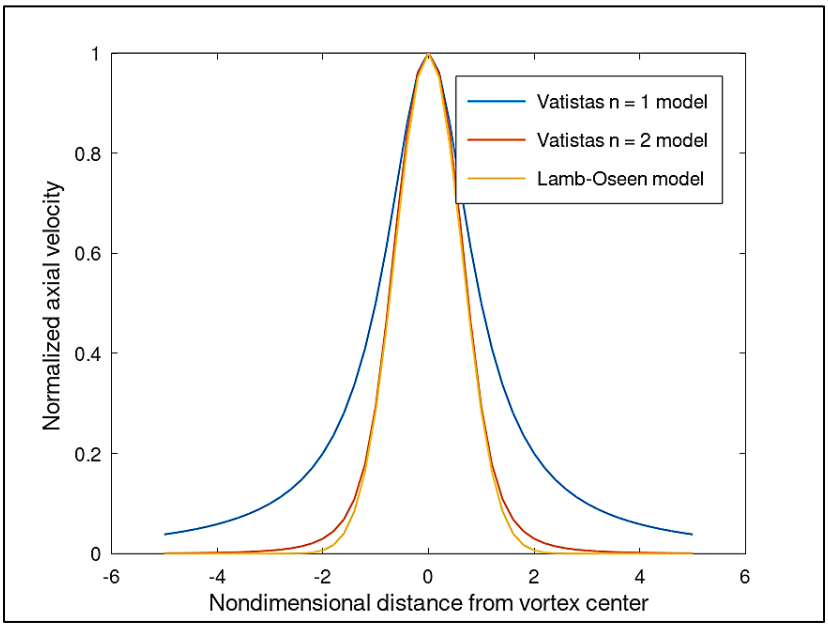


Fig. 4.18. The nondimensional axial velocity ($V_z / V_{z\,max}$) profile for different vortex models

Figures 4.17 and 4.18 depict that both plots are symmetric about the vortex center. The swirl velocity is minimum (zero) and the axial velocity is maximum at the vortex center, which is expected. Results from the vortex models shown in Figs. 4.16–4.18 depicts the vortex center's

minimum swirl velocity and axial velocity. The swirl velocity increases, and axial velocity decreases with the distance from the vortex center to the periphery. This phenomenon is also similar to that reported by Leishman (2006). In addition, the normalized axial and radial displacements reduce by increasing the wake age, as shown in Figs. 4.19 and 4.20, are similar to the phenomena found in the literature (Leishman, 2006).

### 4.4.2 Wake Models for Hovering Flight

The tip vortex position in hover is located by the prescribed Landgrebes wake model and Kocurek & Tangler's wake model. The axial and radial displacements are calculated using Eqs. 18−23 and plotted as shown in Figs. 4.19 and 4.20, respectively. The considered parameters are four-bladed rotor, i.e., $N_b = 4$, $C_T = 0.008$, $A = 0.78$, and $\theta_{tw} = -13°$.

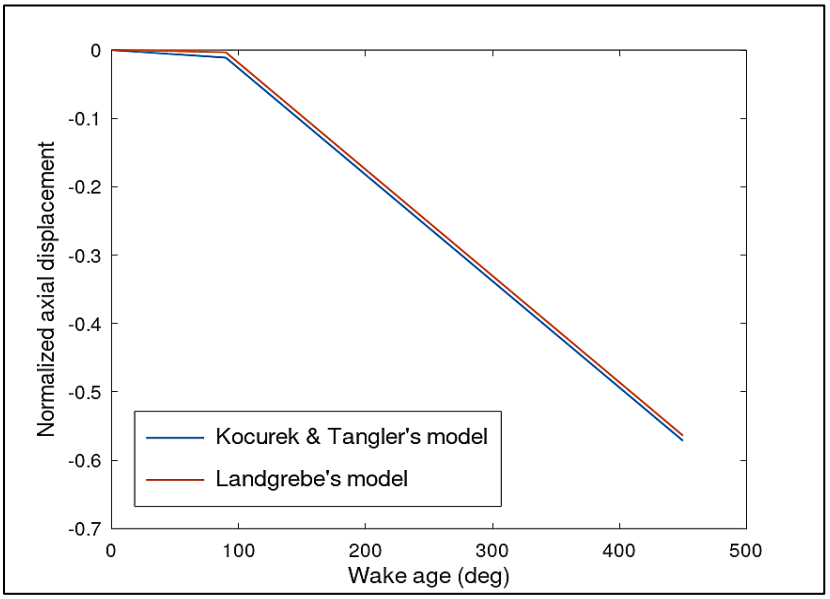


Fig. 4.19. Comparison of normalized axial displacement ($z/R$) with change in wake angle for the prescribed wake models

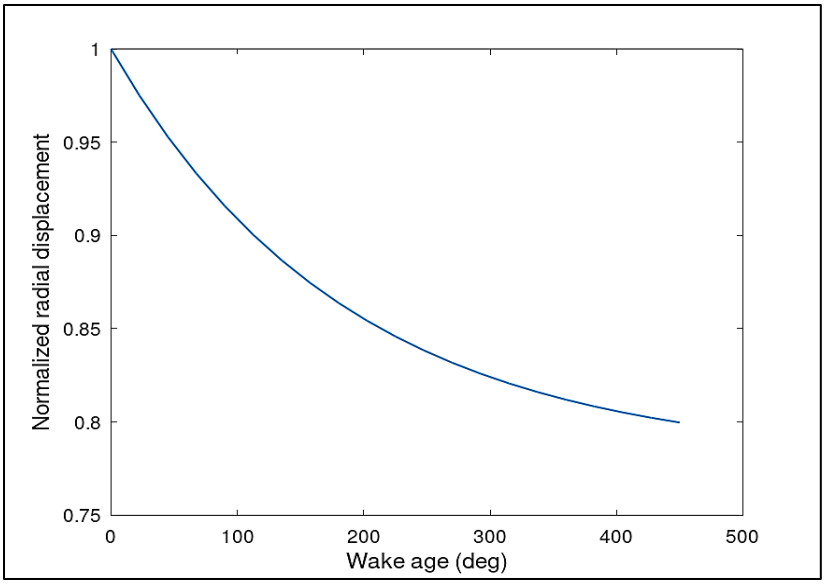


Fig. 4.20. Normalized radial displacement ($y/R$) with change in wake angle for the prescribed wake model

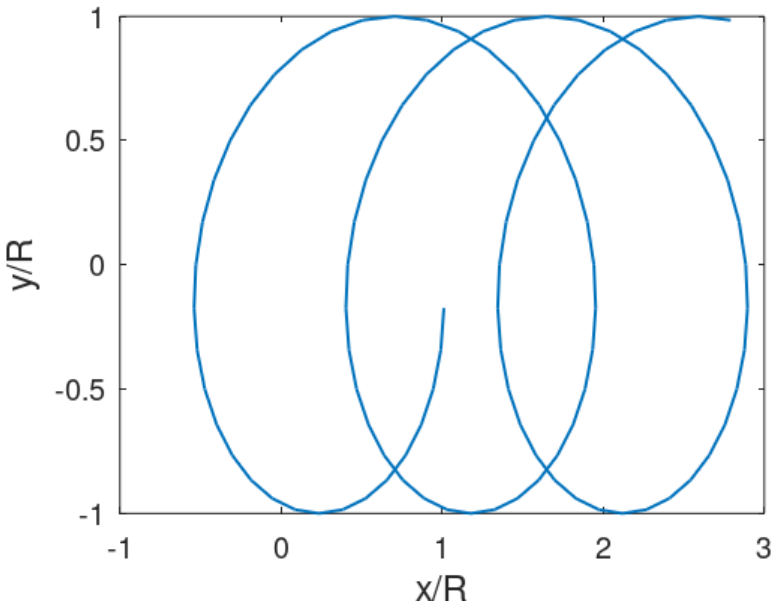


Fig. 4.21. Plane (top) view of the rigid or undistorted wake geometry for forward flight

### 4.4.3 Wake Models for Forward Flight

The representative rigid wake geometry in forward flight obtained using the formulas of rigid or undistorted vortex wake models of the rotor blade are shown in Figs. 4.21 and 4.22 for the plane or top view, and the side view, respectively.

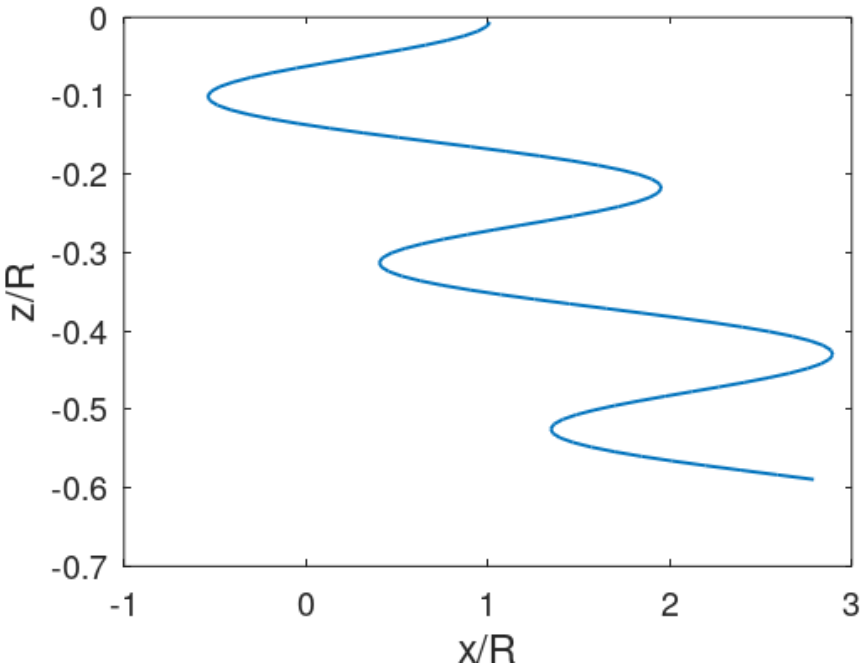


Fig. 4.22. Side view of the rigid or undistorted wake geometry for forward flight

### 4.4.4 Vortex Contours

The output of the FSI simulation enables flow visualization and shows the dynamic characteristics. The velocity magnitude and helicity contours for the Bo 105 helicopter rotor blade are shown in Fig. 4.23 for different angles of attack.

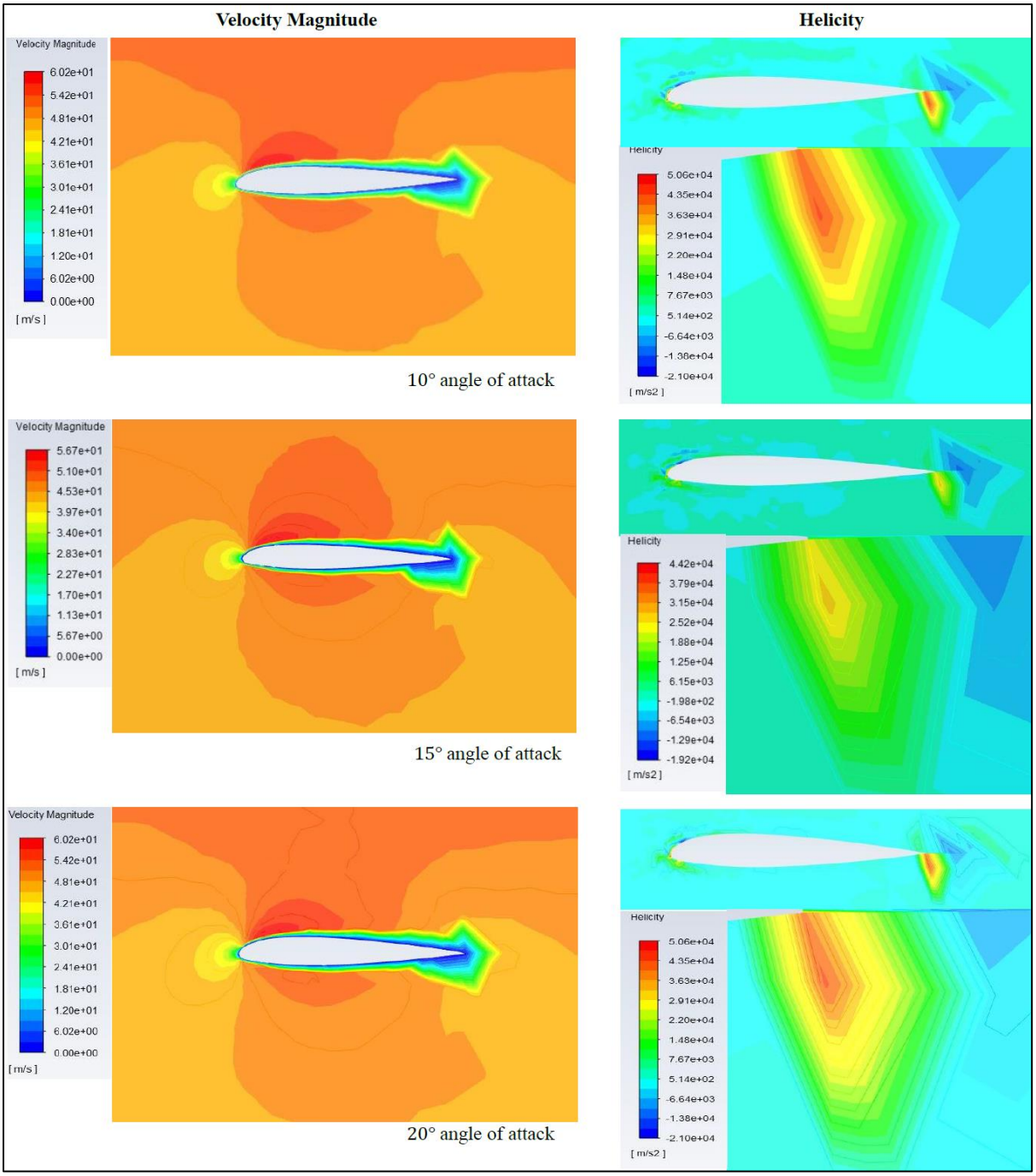


Fig. 4.23. Velocity magnitude and helicity contour plot (alongwith a zoomed in figures near the trailing edge) in x-y plane for the Bo 105 rotor blade near the tip

The velocity magnitude varies with the angle of attack, and the helicity near the trailing edge of the airfoil cross-section shows the vortex structure due to flow over the rotor blade.

# CHAPTER 5

# Conclusions and Future Work

## 5.1 Concluding Remarks

This study aims at characterizing the dynamic behavior of a hingeless MBB Bo 105 helicopter rotor blade. A finite element model is developed to estimate the resonance frequencies and mode shapes in terms of three coupled degrees-of-freedom: flap, lead-lag, and torsional motions. A small-scale rotor blade model is manufactured for the experimental validation of the computational models. The shaker experimental arrangement is used along with the digital image correlation system for the vibration testing of the small-scale model to validate the computational results. A fluid-structure interaction model, comprising the finite element model of the rotor blade and a computational fluid dynamics model of the surrounding fluid flow, is developed for investigating the aerodynamic behavior. A wind tunnel setup is used to obtain aerodynamic properties using the small-scale model and validate relevant computational results. Different models of small-scale rotor blades are also generated to study the sensitivity of the experimental validation. Wake and vortex formation are also outlined by considering different tip vortex models and prescribed wake models for both hovering and forward flights. Finally, the following conclusions can be drawn based on the numerical and experimental results:

1. The torsional and flapping natural frequencies are the highest and the lowest values, respectively, during the vibration of the rotor blade. The lead-lag natural frequencies are higher than the flapping natural frequencies due to the geometry of the airfoil section. The experimental and computational results of natural frequencies and mode shapes show a good agreement for the small-scale rotor blade.

2. The coefficient of lift increases with the angle of attack up to a critical value. The coefficient of drag also increases with the angle of attack. The experimental and computational results of aerodynamic coefficients show a good agreement for the small-scale rotor blade.

3. An understanding of the test installation's impact on the rotor blade's frequencies by a shake test on the conducted wind-tunnel experiment is obtained. The challenges of experimental validation in terms of sensitivity and similarity model are also investigated and depict a reason for deviation of the wind-tunnel experimental outcome.

4. The tangential or swirl and axial velocities with the distance from the vortex center are plotted for the tip vortex core region. At the vortex center, the swirl velocity is minimum, and the axial velocity is maximum. The swirl velocity increases and the axial velocity decreases with increasing the distance from the vortex center to the core radius.

5. The forward flight velocity of the helicopter has a significant influence on the characteristics of the rotor wake. The rotor wake changes as wake fluid are pushed ahead of the rotor into the surrounding still air.

**5.2 Future Work**

In this study, the modal analysis of a helicopter rotor blade is carried out in terms of the resonance frequencies and mode shapes, aerodynamic coefficients at different angles of attack, vortex formation, and wake response at hovering and forward flights. Several modifications are possible in the FSI modeling to attain real scenarios, including the rotation properties. The following recommendations can improve this study:

1.In the operation of a helicopter, rotational characteristics are fundamental. The rotational behavior can be incorporated into the FSI simulation to obtain the aerodynamics and vortex characteristics of the rotor blade. Vibration characteristics can also be obtained in the case

of rotation. The effect of rotation can be analyzed regarding the resonance frequencies, mode shapes, and aerodynamic performances and instabilities.

2.The near-wake due to the close interactions of the rotor blade and the tip vortex can be treated by the lifting surface and the lifting-line theories. The shed vortex line caused by the azimuthal variation in the bound circulation is suggested to be included in the rotor blade aerodynamics.

3. The induced flow behavior causes a change in the flow field near the airfoil. Therefore, the effects of shed vortices are recommended to be included in the aerodynamic studies of the rotor blade.

# References


Aksencer, T., and Aydogdu, M., 2015, “Flapwise vibration of rotating composite beams” Composite Structures, 134, pp. 672–679.

Bailly, J., and Bailly, D., 2019, “Multifidelity Aerodynamic Optimization of a Helicopter Rotor Blade,” AIAA Journal, 57(8), pp. 3132–3144.

Bardera Mora, R., and Matías García, J. C., 2022, “Helicopter Rotor Ground Effect and Frigate Interaction Investigated by Particle Image Velocimetry,” AIAA Journal, 60(1), pp. 129–143.

Bramewell, A. R. S., Balmford, D., and Done, G., 2001, “Bramewell’s Helicopter Dynamics,” Elsevier.

Brown, R. E., 2000, “Rotor wake modeling for flight dynamic simulation of helicopters,” AIAA Journal, 38(1), pp. 57–63.

Cook, J. R., Smith, M. J., Thepvongs, S., and Cesnik, C. E., 2017, “Computational Aeroelasticity of Rotating Wings with Deformable Airfoils,” Journal of the American Helicopter Society, 62(3), pp. 14–26.

Escobar, D., Chopra, I. and Datta, A., 2021, “High-fidelity aeromechanical analysis of coaxial mars helicopter,” Journal of Aircraft, 58(3), pp. 609–623.

Farrugia, R., Sant, T., and Micallef, D., 2016, “A study on the aerodynamics of a floating wind turbine rotor,” Renewable Energy, 86, pp. 770–784.

Fluent, Ansys., 2017, “ANSYS Fluent Theory Guide, Release 18.0,” Ansys Inc.

Goerttler, A., Braukmann, J. N., Schwermer, T., Gardner, A. D., and Raffel, M., 2018, “Tip-vortex investigation on a rotating and pitching rotor blade,” Journal of Aircraft, 55(5), pp. 1792–1804.

Ho, J. C., and Yeo, H., 2017, “Assessment of comprehensive analysis predictions of helicopter rotor blade loads in forward flight,” Journal of Fluids and Structures, 68(2017), pp. 194–223.

Hohenemser, K. H., 1974, “Hingeless rotorcraft flight dynamics,” AGARD-AG-197.

Hodges, D. H., and Ormiston, R. A., 1976, “Stability of elastic bending and torsion of uniform cantilever rotor blades in hover with variable structural coupling,” NASA Technical Note D-8192, Ames Research center, California, USA.

Hodges, D. H., Atilgan, A. R., Fulton, M. V., and Rehfield, L. W., 1991, “Free-vibration analysis of composite beams,” Journal of the American Helicopter Society, 36(3), pp. 36–47.

Hoseini, H. S., and Hodges, D. H., 2019, “Aeroelastic Stability Analysis of Damaged High-Aspect-Ratio Composite Wings,” Journal of Aircraft, 56(5), pp. 1794–1808.

James, S. W., Kissinger, T., Weber, S., Mullaney, K., Chehura, E., Pekmezci, H. H., Barrington, J. H., Staines, S. E., Charrett, T., Lawson, N. J. and Lone, M., 2022, “Fibre-optic measurement of strain and shape on a helicopter rotor blade during a ground run-part 1: measurement of strain,” Smart Materials and Structures, Accepted Manuscript, pp. 1–15.

Johnson, W., 1977, “Calculated Dynamic Characteristics of a Soft-Inplane, Hingeless Rotor Helicopterm,” NASA Technical Memorandum, NASA TM-73, 262, pp. 2–3.

Leishman, J. G., 2006, “Principles of Helicopter Aerodynamics,” Cambridge University Press, Cambridge.

Li, Q., Kamada, Y., Maeda, T., Murata, J., and Nishita, Y., 2016a, “Effect of turbulent inflows on airfoil performance for a horizontal axis wind turbine at low Reynolds numbers (Part II: Dynamic pressure measurement),” Energy, 112, pp. 574–587.

Koning, W. J., Johnson, W., and Grip, H. F., 2019, “Improved Mars helicopter aerodynamic rotor model for comprehensive analyses,” AIAA Journal, 57(9), pp. 3969–3979.

Kim, T., Yun, C., Kee, Y., Kim, S. H. and Jung, S., 2013, “Dynamic Characteristic Study of Hingeless Blade Stiffness Reinforcement for Bearingless Rotor Whirl Tower Test,” Transactions of the Korean Society for Noise and Vibration Engineering, 23(2), pp. 105–111.

Madden, P. A., 1967, “Angle-of-Attack Distribution of a High-Speed Helicopter,” Journal of the American Helicopter Society, 12(2), pp. 41–49.

McAlister, K. W., 2004, “Rotor wake development during the first revolution,” Journal of the American Helicopter Society, 49(4), pp. 371–390.

Patterson, R. P. and Friedmann, P. P., 2022, “Vibration Reduction on Helicopter Rotors Using Open-Loop Flow Control,” AIAA Journal, 60(1), pp. 113–128.

Pulok, M. K. H., Rahman, M. S. and Akanda, M. A. S., 2021, “Numerical analyses of stress and deformation in sandwich-structured composites,” The Journal of Strain Analysis for Engineering Design, 56(6), pp. 339–358.

Pulok, M. K. H., and Chakravarty, U. K., 2022, “Modal Characterization, Aerodynamics, and Gust Response of an Electroactive Membrane,” AIAA Journal, 60(5), pp. 1–12.

Pulok, M. K. H., and Chakravarty, U. K., 2019, “A Study of the Aerodynamics of a Helicopter Rotor Blade,” Proc. ASME International Mechanical Engineering Congress and Exposition, Saltlake City, UT, USA, IMECE2019-11477, pp. 1–9.

Pulok, M. K. H., and Chakravarty, U. K., 2020, “An Investigation of the Aerodynamic and Vibration Behavior of a Helicopter Rotor Blade,” Proc. ASME International Mechanical Engineering Congress and Exposition, Virtual, Online, IMECE2020-23668, pp. 1–11.

Pulok, M. K. H., and Chakravarty, U. K., 2021, “November. An Investigation of the Wake and Vortex Formation of a Helicopter Rotor Blade,” Proc. ASME International Mechanical Engineering Congress and Exposition, Virtual, Online, IMECE2021-70777, pp. 1–10.

Reddy, R. R. K., and Ganguli, R., 2003, “Structural damage detection in a helicopter rotor blade using radial basis function neural networks,” Smart materials and Structures, 12(2), pp. 232–241.

Riyad, I. A., and Chakravarty, U. K., 2018, “An analysis of harmonic airloads acting on helicopter rotor blades,” Proc. ASME International Mechanical Engineering Congress and Exposition, Pittsburg, PA, USA, IMECE2018-86625, pp. 1–11.

Roy, A. M., 2021, “Finite Element Framework for Efficient Design of Three Dimensional Multicomponent Composite Helicopter Rotor Blade System,” Eng, 2(1), pp. 69–79.

Sarker, P., Theodore, C. R., and Chakravarty, U. K., 2016, “Vibration Analysis of a Composite Helicopter Rotor Blade at Hovering Condition,” ASME 2016 International Mechanical Engineering Congress and Exposition, Phoenix, Arizona, USA. IMECE2016-65859, pp. 1–10.

Sarker, P., 2018, “Dynamic Response of a Hingeless Helicopter Rotor Blade at Hovering and Forward Flights,” Ph.D. Thesis, Mechanical Engineering, University of New Orleans, Louisiana, USA.

Sarker, P. and Chakravarty, U. K., 2021, “On the dynamic response of a hingeless helicopter rotor blade. Aerospace Science and Technology,” 115, pp. 106741:1–23.

Sarker, P., and Chakravarty, U. K., 2019, “A Case Study of the Unsteady Response of a Hingeless Helicopter Rotor Blade,” Proc. ASME International Mechanical Engineering Congress and Exposition, Saltlake City, UT, USA, IMECE2019-11084, pp. 1–8.

Schwarz, C., Bauknecht, A., Mailänder, S., and Raffel, M., 2019, “Wake characterization of a free-flying model helicopter in ground effect,” Journal of the American Helicopter Society, 64(1), pp. 1–16.

Schwarz, C., Bauknecht, A., Wolf, C. C., Coyle, A., and Raffel, M., 2020, “A full-scale rotor-wake investigation of a free-flying helicopter in ground effect using BOS and PIV,” Journal of the American Helicopter Society, 65(3), pp. 1–20.

Shinoda, P. M., 2004, “Investigation of a full-scale wide chord blade rotor system in the NASA Ames 40- by 80- foot wind tunnel,” American Helicopter Society 4th Decennial Specialist’s Conference on Aeromechanics, San Francisco, California, USA.

Singh, P., and Friedmann, P. P., 2018, “Application of vortex methods to coaxial rotor wake and load calculations in hover,” Journal of Aircraft, 55(1), pp. 373–381.

Uluocak, S., Perçin, M., and Uzol, O., 2021, “Experimental investigation of tip anhedral effects on the aerodynamics of a model helicopter rotor in hover,” Aerospace Science and Technology, 113, p.106671.

Van der Wall, B. G., and Van der Wall, L. B., 2017, “Analytical estimate of rotor controls required for a straight vortex disturbance rejection,” Journal of the American Helicopter Society, 62(1), pp. 1–4.

van der Velden, W. C. P., Romani, G. and Casalino, D., 2021. Validation and insight of a full-scale S-76 helicopter rotor using the Lattice-Boltzmann Method. Aerospace Science and Technology, 118, p.107007.

Vatistas, G. H., Kozel, V., Mih, W. C., 1991, “A simpler model for concentrated vortices,” Exp. Fluids, 11(1), pp. 73–76.

Venegas, E. D., Rieu, P., and Le Dizès, S., 2021, “Structure and stability of Joukowski's rotor wake model,” Journal of Fluid Mechanics, 911(A6), pp. 1–26.

Vouros, S., Goulos, I., Scullion, C., Nalianda, D. and Pachidis, V., 2021, “Impact of Tip-Vortex Modeling Uncertainty on Helicopter Rotor Blade–Vortex Interaction Noise Prediction,” Journal of the American Helicopter Society, 66(1), pp. 1–13.

Yang, X., Yang, A., and Si, J., 2015, “Efficient numerical techniques for simulating a rotocraft flowfield with overlapping grids,” AIAA Journal, 53(5), pp. 1372–1383.

Walsh, J. L., Bingham, G. J., and Riley, M. F., 1987, “Optimization methods applied to the aerodynamic design of helicopter rotor blades,” Journal of the American Helicopter Society, 32(4), pp. 39–44.

Wang, X., Trollinger, L., Chopra, I., 2020, “Refined Performance Results on a Slowed Mach-Scaled Rotor at High Advance Ratios,” Journal of the American Helicopter Society, 65(1), pp. 1–13.

Weiss, A., Gardner, A. D., Schwermer, T., Klein, C., and Raffel, M., 2019, “On the effect of rotational forces on rotor blade boundary-layer transition,” AIAA Journal, 57(1), pp. 252–266.

White, J. R., Adams, D. E., and Rumsey, M. A., 2011, “Modal Analysis of CX-100 Rotor Blade and Micon 65/13 Wind Turbine,” Structural Dynamics and Renewable Energy, Conference Proceedings of the Society for Experimental Mechanics Series. Springer, New York, NY, 1, pp. 15–27.

Wirth, N., Bayrasy, P., Landvogt, B., Wolf, K., Cecutti, F., and Lewandowski, T., 2017, “Analysis and Optimization of Flow Around Flexible Wings and Blades Using the Standard Co-

simulation Interface MpCCI," Recent Progress in Flow Control for Practical Flows. Springer, Cham, pp. 283–321.

Wolf, C. C., Schwarz, C., Kaufmann, K., Gardner, A. D., Michaelis, D., Bosbach, J., Schanz, D., and Schröder, A., 2019, "Experimental study of secondary vortex structures in a rotor wake," Experiments in Fluids, 60(11), pp. 1–16.

Zaw, M. T., Tun, H. M., and Naing, Z. M., 2014, "Development of mathematical model and stability analysis for UAH," International Journal of Scientific and Research Publications, 4(5), pp. 1–10.

Zhao, J., 2005, "Dynamic Wake Distortion Model for Helicopter Maneuvering Flight," Ph.D. Thesis, School of Aerospace Engineering, Georgia Institute of Technology.

Zhou, X., He, S., Dong, L. and Atluri, S. N., 2022, "Real-Time Prediction of Probabilistic Crack Growth with a Helicopter Component Digital Twin," AIAA Journal, 60(4), pp. 1–13.

Zhou, Z., and Huang, J., 2022, "Numerical investigations on radar cross-section of helicopter rotor with varying blade pitch," Aerospace Science and Technology, 123, pp.107452.

## VITA

The author was born in a village of Pabna, Bangladesh and passed his primary and secondary school from there, and moved to Dhaka, the capital of Bangladesh for his higher secondary study. He went to Rajshahi, Bangladesh, and obtained his Bachelor's degree in Mechanical Engineering in 2011 from the Rajshahi University of Engineering and Technology. He also completed his Master of Science degree from Bangladesh University of Engineering and Technology in 2016. Meanwhile, after completion of his Bachelor's degree, he joined the Aeronautical College of Bangladesh, Dhaka, Bangladesh in October 2011 and served there up to April 2012 as a Lecturer in Mechanical Engineering. He joined BASIC Bank Limited in May 2012 and worked as an Assistant Manager for over four years before coming to the USA. He joined the University of New Orleans to pursue his Ph.D. in Fall 2016. He finished his Ph.D. in the Engineering and Applied Sciences, Mechanical Engineering concentration in Summer 2022.